Construction and Building Materials 540 (2026) 147729

Contents lists available at ScienceDirect

Construction and Building Materials

journal homepage: www.elsevier.com/locate/conbuildmat

Rheological performance, damage resistance, and processing effects in a multi-additive modified binder

Foad Ghasemi [a], Ehsan Yaghoubi [a,b,*], Rudi van Staden [a,b], Ali Rajabipour [c], Ramin Shahbazi [c], Ali Rahman [d]

[a] Institute for Sustainable Industries and Liveable Cities, Victoria University, Melbourne, Australia
[b] College of Sport, Health and Engineering, Victoria University, Melbourne, VIC 3011, Australia
[c] Centre for Asphalt and Road Technologies (CART), Charles Darwin University, Darwin, Australia
[d] University of Leeds, Leeds, UK

ARTICLE INFO

Keywords:
Bitumen modification
Microwave-activated crumb rubber
Wollastonite
Iron oxide
Taguchi design
Multi-response optimization

ABSTRACT

Multi-additive modification of bitumen is increasingly adopted to tune rheological performance, but the combined influence of rigid mineral/oxide phases and elastomeric modifiers, along with the way processing conditions shape rutting–fatigue trade-offs, is still not fully understood. This study examines the behavior of bitumen co-modified with iron (III) oxide (Fe_2O_3), wollastonite ($CaSiO_3$), and microwave-activated crumb rubber (MACR), using a Taguchi L25 design to screen six formulation and processing variables. Twenty-five modified binders, and a neat (unmodified) binder as reference, were characterized through conventional binder tests and dynamic shear rheometer (DSR) measurements, frequency sweep, Multiple Stress Creep Recovery (MSCR), and Linear Amplitude Sweep (LAS). Microstructural analysis was conducted to determine whether the performance changes were driven by chemical interactions or primarily by the distribution and dispersion of additives within the binder. The results show that MACR exerts the strongest influence on MSCR outcomes and high-temperature viscoelastic behavior, while fatigue-related indicators appear more sensitive to processing, especially mixing temperature, and shear intensity. Because the measured responses did not improve together, the competing performance indicators were evaluated within a multi-response framework. The neat binder retained the highest LAS life at 15% strain, demonstrating that improved rutting resistance did not translate directly into large-strain damage tolerance. A desirability model, ranking under Dirichlet-distributed weight uncertainty, and Pareto screening identified U6 (2% Fe_2O_3, 5% wollastonite, 12% MACR, 185 °C, 60 min, 6000 rpm) as the leading screening candidate. U6 achieved $J_{nr,3.2} = 0.49$ kPa^{-1}, $R_{3.2} = 14.78\%$, a geometric-mean LAS fatigue-life metric $N_{f,geo} \approx 953$, and composite desirability $D = 0.6869$. These findings provide a starting point for subsequent work on aged binders, mixture-scale validation, and the incorporation of additional functional additives such as fire-retardant or anti-aging modifiers.

1. Introduction

Modern asphalt pavements are increasingly required to perform under heavier traffic loads and wider thermal fluctuations, yet conventional paving-grade bitumen remains highly susceptible to temperature. At elevated temperatures, asphalt mixture softens and becomes more prone to rutting, whereas at lower and intermediate temperatures it stiffens and turns more brittle, accelerating fatigue damage and thermal cracking. This basic tension in performance has kept binder modification at the center of asphalt research, particularly approaches aimed at improving resistance to permanent deformation without creating excessive trade-offs in workability or damage tolerance [1,2].

Among these approaches, crumb rubber (CR) derived from end-of-life tires remains one of the most established modifiers, as it can enhance elasticity and offers a practical route for waste reutilization [3–5]. During blending, CR is known to absorb the lighter maltene fractions and swells, which typically raises viscosity and stiffness while also improving elastic recovery [6,7]. Those benefits, however, may

* Corresponding author at: Institute for Sustainable Industries and Liveable Cities, Victoria University, Melbourne, Australia.
E-mail addresses: Foad.ghasemi@live.vu.edu.au (F. Ghasemi), Ehsan.yaghoubi@vu.edu.au (E. Yaghoubi), Rudi.VanStaden@vu.edu.au (R. van Staden), Ali.rajabipour@cdu.edu.au (A. Rajabipour), ramin.shahbazi@cdu.edu.au (R. Shahbazi), A.Rahman1@leeds.ac.uk (A. Rahman).

https://doi.org/10.1016/j.conbuildmat.2026.147729
Received 21 May 2026; Received in revised form 21 July 2026; Accepted 5 August 2026
Available online 10 August 2026

come with disadvantages such as storage instability caused by phase separation and the elevated viscosity that can make mixing and compaction more difficult [8,9]. Equally important, improvements in rutting resistance do not consistently carry over to fatigue resistance, especially in cases where stiffening becomes the dominant response [10].

Microwave activation has therefore been proposed as a pretreatment method to enhance the performance of CR in bitumen [11]. By generating rapid volumetric heating, microwave treatment can produce surface cracking and partial devulcanization within CR particles, which in turn increases surface roughness and creates additional interaction sites on the particle surface. These changes may improve the compatibility of CR with bitumen and lessen the tendency toward phase separation [12]. Earlier studies have reported that microwave-activated crumb rubber (MACR) can enhance high-temperature rheological behavior and, in some cases, aging resistance relative to systems containing untreated rubber. Even so, the reported outcomes are not fully consistent, since they depend on activation conditions, rubber gradation, blending temperature, and shear history [13,14]. The basis of these changes is still not fully clear, particularly when MACR is used alongside other modifiers.

Mineral and oxide additives have also been studied as reinforcement-type modifiers that increase stiffness and limit flow [15]. Wollastonite ($CaSiO_3$) can improve stiffness and resistance to deformation through particle interlocking and more efficient stress transfer, although excessive stiffening may also increase susceptibility to cracking if the formulation is not carefully balanced [16]. Iron(III) oxide (Fe_2O_3) has similarly been linked to gains in stiffness and deformation resistance in asphalt materials. At the binder scale, these effects are generally interpreted in terms of physical reinforcement and interfacial interactions rather than substantial chemical transformation [17]. Such additives are therefore plausible complements to rubber-modified systems, yet their combined behavior with MACR has not been studied.

Hybrid crumb-rubber/mineral binders are already established in the literature. Nanoclay has been incorporated into asphalt rubber to investigate storage stability and rheology [18], microwave-activated rubber has been combined with nanosilica to examine high-temperature behavior and interaction mechanisms [19], and crumb-rubber/nanocomposite-clay binders have been evaluated under different curing and blending conditions [20]. These studies demonstrate that secondary inorganic phases and processing history can influence the phase stability and rheological response of rubberized binders. However, these effects are system-specific, the behavior of layered clays or nanosilica cannot be assumed to transfer directly to acicular wollastonite and Fe_2O_3.

The selection of the three modifiers was based on a testable performance hypothesis. MACR was selected because rubber swelling and elastic response can contribute to recoverable deformation, wollastonite was selected because its acicular calcium-silicate morphology offers morphology-based reinforcing potential, and Fe_2O_3 was selected because previous binder studies reported increased softening point and complex modulus together with improved J_{nr}- and rutting-related behavior [15–17,21–23].

Microwave activation has been reported to roughen the crumb-rubber surface and promote partial cleavage of S–S and C–S bonds, thereby affecting rubber swelling, surface activity, and compatibility with bitumen [11–14]. These effects are sensitive to microwave exposure and subsequent blending conditions. The present rationale therefore does not presume that MACR, wollastonite, and Fe_2O_3 act independently or interact favorably. Their simultaneous use may produce competitive, synergistic, antagonistic, or processing-induced effects involving binder-fraction uptake, particle wetting, adsorption, agglomeration, interfacial reorganization, or minor oxidation.

Wollastonite ($CaSiO_3$), an acicular calcium-silicate mineral, was selected as a potential reinforcing phase capable of increasing consistency and supporting stress transfer through particle interlocking, whereas Fe_2O_3 was selected as a rigid oxide phase capable of restricting viscous flow [17,21,23]. Their use with MACR was motivated by functional complementarity: the rubber phase was expected to govern swelling, elastic recovery, and high-temperature viscoelasticity, while the mineral and oxide phases provided secondary reinforcement. Microwave treatment can create cracks and porosity and can partially devulcanize rubber by disrupting sulfur-containing C–S and S–S cross-links, thereby increasing surface roughness, available surface area, and surface activity and changing the uptake of lighter bitumen fractions during swelling [11,13,14,19,24]. These surface changes provide a plausible basis for altered wetting or retention of wollastonite and Fe_2O_3 near rubber–binder interfaces. This is treated as a working hypothesis. The rationale does not presume that the three modifiers act independently or that their combination is chemically inert. Competitive, synergistic, and processing-induced interactions remain possible, accordingly, FTIR and local SEM/EDS observations are used to assess consistency with possible interactions.

Accordingly, the purpose of this study was to map the coupled formulation–processing response and the resulting performance trade-offs rather than to assign a unique reaction pathway.

The knowledge gap is not purely compositional, since binder performance is shaped by the coupled effects of formulation and processing variables, including additive dosage, blending temperature, mixing duration, and shear conditions [25]. Because these factors do not operate independently, asphalt binder research has increasingly relied on structured experimental design to screen variables efficiently and identify robust formulation windows [26]. Taguchi design is especially useful at the binder scale, since orthogonal arrays allow multiple factors to be screened with limited experimental availabilities [27,28]. In asphalt studies, Taguchi methods are often used alongside signal-to-noise (S/N) analysis and analysis of variance (ANOVA) to identify the factors most strongly affecting penetration, softening point, viscosity, modulus, phase angle, and related indicators [29–32]. Their use has been particularly common in CR-modified, polymer-modified, and filler-enhanced binders, especially in cases where modifier dosage serves as the main control variable and processing conditions exert a secondary, though still meaningful, effect [27,30,31,33].

At the same time, the Taguchi literature has long acknowledged the method's limitations. Orthogonal arrays are efficient for estimating main effects, but higher-order interactions are often confounded unless the design is set up specifically to disentangle them. This is particularly consequential in hybrid binders, where performance may be governed by synergistic or antagonistic interactions among modifiers [27,34]. Another recurring issue concerns multi-response optimization. Asphalt binders are expected to meet competing requirements related to rutting, fatigue, and durability, yet many studies still treat each response in isolation or combine several responses into a single index without stating the underlying trade-offs explicitly or testing whether the selected formulation remains stable when response priorities change [35–37]. This is particularly important in binder selection, where the importance assigned to rutting resistance, elastic recovery, fatigue tolerance, stiffness, and chemical indicators is not constant across applications. For that reason, Taguchi design is better understood as an efficient tool for screening and early-stage optimization than as a complete framework for mechanistic modeling or uncertainty-aware decision-making [38,39].

Although the performance and modification mechanisms of crumb rubber, wollastonite, and iron oxides continue to be studied individually, no systematic binder-scale assessment has jointly mapped MACR, wollastonite, and Fe_2O_3 across both composition and processing variables. Composition and processing must be considered together because rubber swelling, binder-fraction uptake, particle wetting, agglomerate breakup, and interfacial development occur concurrently. The present Taguchi L25 study jointly screens three modifier dosages and three processing factors and uses conventional tests, frequency sweep, MSCR, LAS, FTIR, and local SEM/EDS to compare the resulting formulation–processing states. An uncertainty-aware multi-response workflow is then used to identify conditional performance compromises [40–44].

The specific gap is the integrated mapping of a three-phase MACR–wollastonite–Fe_2O_3 binder in which all three modifier dosages and the principal thermal–shear processing variables are varied within one experimental design. Existing hybrid studies have generally focused on one secondary inorganic modifier and narrower objectives such as storage stability or high-temperature response [18–20], whereas the wider MACR literature demonstrates that mixing temperature, duration, shear speed, and rubber pretreatment jointly govern swelling, degradation, and rheological response [24]. The present Taguchi L25 study therefore screens three modifier-dosage factors and three processing factors together, compares conventional properties, frequency-sweep, MSCR, LAS, FTIR, and local SEM/EDS responses, and applies uncertainty-aware multi-response and Pareto analyses to examine rutting–recovery–fatigue trade-offs. The contribution is thus a coupled composition–processing screening and decision framework for this specific material system.

2. Materials and methods

Fig. 1 outlines the overall workflow, which is discussed in more detail in the sections that follow. Each section (row) of Fig. 1 addresses a specific part of the methodology, including material selection, experimental design, binder preparation, testing procedures, and the multi-response decision-making process. Taken together, they offer a sequential account of how the final formulation was evaluated and selected.

2.1. Materials

A Class 320 (C320) bitumen, widely used in Australian road pavements, was adopted as the base (neat) binder, and its properties are listed in Table 1.

Wollastonite ($CaSiO_3$) and Fe_2O_3 both passed a 0.075 mm (75 μm) sieve. Wollastonite was used as an acicular mineral reinforcement, while Fe_2O_3 was used as a rigid oxide phase with potential filler-like and interfacial effects [17,21–23]. The crumb rubber had a nominal 30-mesh size (approximately 600 μm) and was microwave-activated before blending. The crumb rubber was first dried at 60 °C for 30 min, then exposed to microwave irradiation at 800 W for 90 s and subsequently stored in a desiccator for 24 h before use. This pretreatment was intended to modify the rubber surface structure and thereby improve its compatibility with bitumen [45,46]. The modifier powders and the

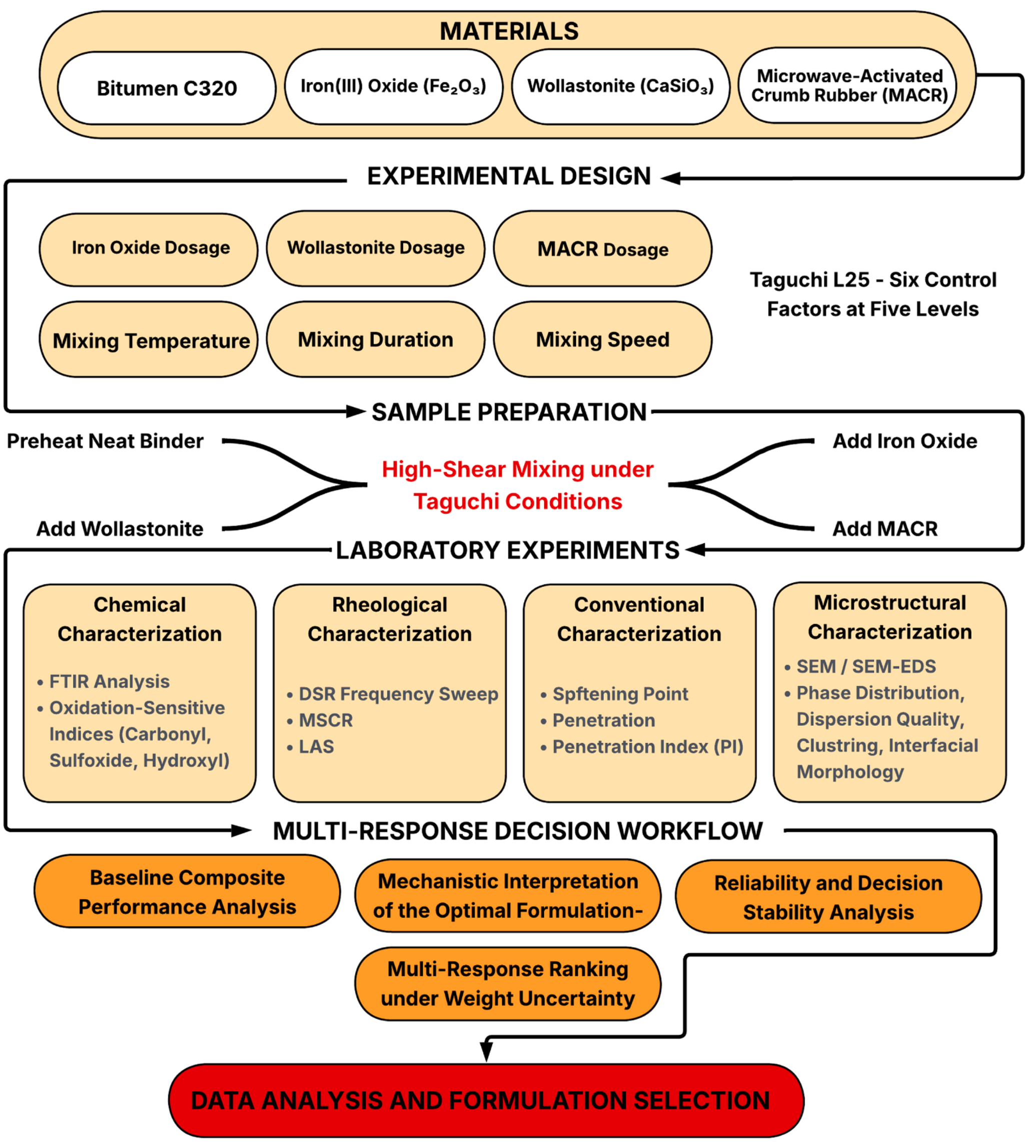

Fig. 1. This study's workflow.

Table 1
Properties of the neat binder.

Characteristics	Standard	Experimental values
Viscosity at 135 °C (Ps.s)	AS 2341.4	0.60
Viscosity at 60 °C (Ps.s)	AS 2341.2	632
Penetration at 25 °C [100 g, 5 s], (0.1 mm)	AS 2341.12	69
Fuming Intensity Index	NRDL-ITM−003	1
Smoke Point Test	NRDL-ITM−004	205
Density at 15 °C (kg/m^3)	AS 2341.7	1048.8
Matter Insoluble in Toluene (%mass)	AS 2341.8	0.0
Flashpoint, Cleveland Open Cup (°C)	ASTM D92	> 350

microwave activation procedure are presented in Figs. 2 and 3.

2.2. Experimental design using Taguchi method

A Taguchi design of experiments was used to study the combined influence of composition and processing conditions without making the test matrix impractically large [47]. This method was selected because it offers a compact and reasonably balanced screening framework for systems governed by multiple control factors, making it possible to examine the main effects of additive dosage and processing variables without the large experimental burden of a full factorial design. Comparable Taguchi-based approaches have been applied in bitumen and asphalt-material optimization when multiple formulation variables need to be screened efficiently under limited laboratory resources [27,36].

Six control factors were examined: Fe_2O_3 dosage, wollastonite dosage, MACR dosage, mixing temperature, mixing duration, and rotational speed. The five levels assigned to each factor were literature-informed. The Fe_2O_3 levels were established from studies of ferric-oxide- and metal-oxide-modified binders [17,23], the wollastonite levels from research examining wollastonite as a bituminous or mineral reinforcement [21,22], and the MACR levels from wet-process and microwave-activated crumb-rubber studies [11–14,45,46].

The processing levels 155, 165, 170, 175, and 185 °C, 10, 20, 30, 45, and 60 min, and 1000, 2000, 3000, 4500, and 6000 rpm, were selected by considering the preparation conditions reported across these additive-modification studies [11–14,17,21,23,45,46], together with the operating range of the laboratory equipment and binder-handling feasibility. These settings represent discrete low-to-high screening conditions within the Taguchi L25 design [47].

Six control factors were considered: Fe_2O_3 content, wollastonite content, MACR content, mixing temperature, duration, and rotational speed. Each was studied at five discrete levels (Table 2). Modifier contents are reported as wt% of the total binder blend, this mass basis differs from mineral-filler contents expressed relative to aggregate or total

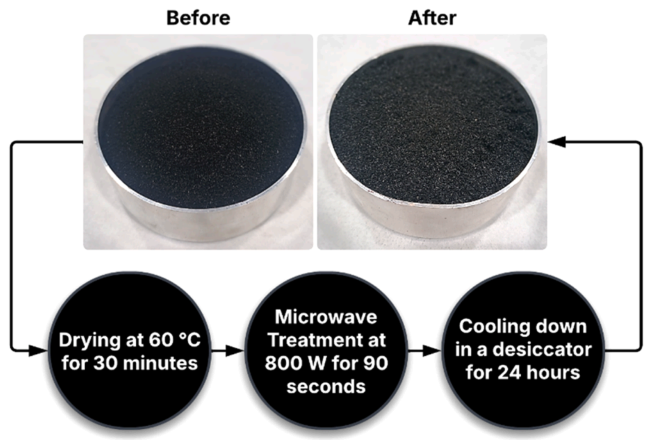

Fig. 3. Microwave activation process of crumb rubber.

Table 2
Parameters and levels considered in the Taguchi design.

	Level 1	Level 2	Level 3	Level 4	Level 5
Iron (III) oxide (Fe_2O_3, wt%)	2	4	6	8	10
Wollastonite (%)	1	2	3	4	5
MACR (wt%)	4	6	8	10	12
Mixing temperature (°C)	155	165	170	175	185
Mixing duration (minutes)	10	20	30	45	60
Mixing rotational speed (rpm)	1000	2000	3000	4500	6000

Name(s)	Wollastonite Calcium Metasilicate, Calcium Silicate Mineral, $CaSiO_3$
Proportion	98% min
Physical description	Fine white powder with no odour
Company	PELTECH Pty Ltd

a

Name(s)	Iron (III) Oxide, RIO REST, Fe_2O_3
Proportion	100%
Physical description	Solid, red, orourless
Exposure limits (OES TWA)	5 mg/m3 (as Fe)
Melting point	> 1000 °C
Supplier	Prince Minerals Australia Pty Ltd

b

Fig. 2. Modifier powders: (a) wollastonite, and (b) iron(III) oxide (Fe_2O_3).

asphalt mixture, and the numerical percentages are therefore not directly equivalent. The dosage bounds were selected primarily as literature-informed laboratory screening limits. Nano-Fe_2O_3 has previously been evaluated at 1%, 3%, and 5% in bitumen [17], while hematite and other iron-oxide modifiers have been examined at 5–30 parts by mass per 100 parts of base bitumen (phr), including 10 phr (equivalent to approximately 9.1 wt% of the total modified-binder blend) [23]. A binder-scale nanowollastonite study reported an optimum close to 4% [21]. Accordingly, 10 wt% Fe_2O_3 and 5 wt% wollastonite were selected as deliberately severe upper screening levels intended to reveal excessive reinforcement, agglomeration, or deterioration of damage tolerance. Because particle characteristics and dosage bases differ among the cited studies, these values provide literature precedent for the investigated order of magnitude.

All modified binders remained sufficiently mobile for laboratory mixing and pouring under their assigned preparation conditions. Its successful laboratory preparation demonstrates only laboratory-scale handling feasibility. Therefore, the upper factor levels are interpreted as screening bounds, and practical production and constructability at these dosages require viscosity-controlled binder testing and mixture-scale validation.

A full factorial design would require $5^6 = 15,625$ experimental combinations. To reduce this burden while preserving balanced coverage of the design space, an L25 orthogonal array was used. This design enables efficient screening of the main effects of the selected factors, but higher-order interactions cannot be estimated separately unless they are explicitly assigned within the array. The OA produced 25 modified binders (U2–U26). A neat binder (U1) was retained as the reference, giving 26 binders in total (Table 3).

For each response, the conventional Taguchi smaller-is-better or larger-is-better S/N expression was selected [27,47]. Because each DSR response was measured once per formulation, the resulting S/N value is only a monotonic transformation of that single observation.

2.3. Binder preparation

All binders were prepared using a Silverson L5M-A laboratory high-shear mixer equipped with a rotor–stator workhead and a square-hole high-shear screen. Each batch was prepared in an individual tapered stainless-steel vessel with an upper diameter of approximately 104 mm, a base diameter of 67 mm, a height of 175 mm, and a nominal capacity of 887 mL. The estimated batch mass was approximately 500 g. Neat C320 binder was heated at 150 °C for 60 min to obtain a pourable condition and was then brought to the run-specific target temperature. During mixing, the vessel was actively heated on a hot plate, but temperature control was manual. A thermocouple was inserted periodically to check the binder temperature. Fe_2O_3 and wollastonite were added gradually, followed immediately by MACR. The vessel opening was covered around the mixer shaft as far as practicable to reduce heat loss and direct air exposure. Nitrogen or another inert gas was not used. After mixing, each formulation remained in its individual vessel, cooled naturally to room temperature, and was stored under ambient laboratory conditions.

The 25 formulations were prepared over approximately two weeks. Testing was subsequently conducted by method for the complete sample set: penetration and softening point were tested first, followed by FTIR, SEM/EDS, and finally DSR frequency sweep, MSCR, and LAS. Binders were reheated only as required to pour or form specimens for the relevant tests.

2.4. Conventional binder tests

Conventional tests were carried out on neat and modified binders. Penetration at 25 °C was measured in accordance with AS 2341.12, and softening point was measured in accordance with AS 2341.18 [48,49]. Both tests were performed in triplicate and mean values are reported. The penetration index (PI) was calculated from penetration P (0.1 mm) and softening point SP (°C) using the Pfeiffer–Van Doormaal relationship shown below. Higher PI values indicate lower temperature susceptibility [50,51]. PI is used as a supplementary consistency descriptor rather than a direct stiffness measurement.

$$PI = \frac{1952 - 500\log_{10}(P) - 20SP}{50\log_{10}(P) - SP + 120} \quad (1)$$

2.5. Rheological testing

Rheological characterization was conducted using an Anton Paar MCR 302e DSR. Frequency-sweep, MSCR, and LAS protocols were performed once for each of the 26 binders, comprising the neat reference

Table 3
Taguchi L25 orthogonal array and corresponding binder formulations.

Sample ID	Fe_2O_3 (wt%)	Wollastonite (wt%)	MACR (wt%)	Mixing temperature (°C)	Mixing duration (min)	Mixing speed (rpm)
U2	2	1	4	155	10	1000
U3	2	2	6	165	20	2000
U4	2	3	8	170	30	3000
U5	2	4	10	175	45	4500
U6	2	5	12	185	60	6000
U7	4	1	6	170	45	6000
U8	4	2	8	175	60	1000
U9	4	3	10	185	10	2000
U10	4	4	12	155	20	3000
U11	4	5	4	165	30	4500
U12	6	1	8	185	20	4500
U13	6	2	10	155	30	6000
U14	6	3	12	165	45	1000
U15	6	4	4	170	60	2000
U16	6	5	6	175	10	3000
U17	8	1	10	165	60	3000
U18	8	2	12	170	10	4500
U19	8	3	4	175	20	6000
U20	8	4	6	185	30	1000
U21	8	5	8	155	45	2000
U22	10	1	12	175	30	2000
U23	10	2	4	185	45	3000
U24	10	3	6	155	60	4500
U25	10	4	8	165	10	6000
U26	10	5	10	170	20	1000

binder U1 and the 25 modified binders U2–U26 generated by the Taguchi L25 array. The L25 array was used as an exploratory screening design. Although each factor level occurs in five different trials and therefore permits comparison of factor-level means and relative main-effect contributions under an additive-effect assumption, these occurrences represent different formulation–processing combinations and are not independent replicates of the same binder.

The single-measurement strategy was adopted because testing 26 binders using frequency-sweep, MSCR, and LAS protocols resulted in an extensive rheological program. Pilot repeatability checks and previous testing of comparable modified binders using the same Anton Paar MCR 302e rheometer provided confidence in instrument and procedural consistency [52,53]. However, instrument repeatability does not replace independent replication and does not quantify variability arising from binder preparation, sampling, specimen formation, storage, or reheating. Accordingly, the calculated S/N values were used only as response-ranking metrics and were not interpreted as measures of robustness against experimental variability. The ANOVA-style sums-of-squares decompositions were used descriptively to partition the observed response variation and rank relative factor contributions. Any pooled residual represents variation not assigned to the retained main-effect terms and may contain interactions, omitted factors, storage/reheating effects, and measurement variability.

To minimize procedural variability, geometry, gap, temperature, equilibration, loading, trimming, reheating, and timing conditions were kept consistent within each method. A run was repeated only when invalidated by an identifiable experimental artifact, such as visible slippage, loss of plate contact, or an instrument discontinuity. Such repetitions replaced invalid runs and were not treated as independent experimental replicates. The DSR results, factor contributions, and multi-response rankings are therefore interpreted as screening-level contrasts within the investigated dataset.

2.5.1. Frequency sweep

Linear viscoelastic behavior was evaluated by frequency sweep over 0.2–30 Hz at 5, 15, 25, 40, 60, and 80 °C [54,55].

Tests at 5, 15, and 25 °C were conducted using an 8 mm parallel-plate geometry with a 2 mm gap and 0.05% strain, whereas tests at 40, 60, and 80 °C were conducted using a 25 mm parallel-plate geometry with a 1 mm gap and 0.1% strain.

2.5.2. Multiple stress creep recovery

High-temperature permanent deformation resistance was evaluated by MSCR at 60 °C following AASHTO [56], using 25 mm plates with a 1 mm gap. The test sequence consisted of twenty creep-recovery cycles at 0.1 kPa, followed by ten cycles at 3.2 kPa, with each cycle including 1 s of creep loading and 9 s of recovery. Percent recovery (R%) and non-recoverable creep compliance (J_{nr}) were taken as the principal response variables, representing elastic recovery and susceptibility to permanent deformation, respectively.

2.5.3. Linear amplitude sweep

Resistance to fatigue-related damage was examined at 25 °C using the AASHTO LAS procedure [57]. Each test began with a small-amplitude frequency sweep at 0.1% strain and was then followed by a strain-controlled amplitude sweep at 10 Hz, with strain increasing from 0.1% to 30% over 310 s. Viscoelastic Continuum Damage (VECD) analysis was applied to derive α (damage evolution parameter), the damage characteristic curves, and the strain-life parameters used for fatigue life (N_f) estimation. Because LAS-derived N_f can be sensitive to specimen preparation and to nonlinear behavior at high strain, test validity was assessed by verifying stable plate contact, the absence of visible edge slip or premature edge fracture, a smooth progression of $|G^*|$ and phase angle during loading, and the absence of abnormal torque or noise discontinuities. Runs that showed clear artefacts, including loss of contact, irregular jumps in phase angle, edge slip, or nonphysical fluctuations in stiffness, were repeated when necessary.

2.6. FTIR characterization

FTIR spectroscopy [58] was employed to examine changes in the functional groups of the modified binders relative to the neat binder, with emphasis on bands typically linked to oxidation-related species in bitumen. Spectra were collected using a single-bounce ATR accessory over the range 4000–600 cm^{-1} at a resolution of 4 cm^{-1}, with 24 scans recorded for each sample. An identical baseline-correction procedure was applied to all spectra. Since ATR-FTIR absorbance intensity is sensitive to sample-crystal contact, applied pressure, and surface condition, quantitative assessment was based on calculated FTIR indices rather than absolute peak intensities alone. The analysis centered on the dominant hydrocarbon profile together with the carbonyl, sulfoxide, and hydroxyl regions, from which comparative indices were derived.

2.7. Microstructural characterization

SEM was employed to examine formulation-dependent morphology, phase heterogeneity, and agglomeration within the binder matrix [59]. The samples were mounted on standard stubs and sputter-coated with Gold/Palladium for 30 s to minimize charging. Imaging was carried out using a Phenom XL G2 desktop SEM in both backscattered (BSD) and secondary electron (SED) modes at approximately 630 ×, 5000 ×, and 30,000 × under fixed operating conditions (15 kV, ~ 39.7 mm working distance, ~ 0.10 Pa chamber pressure). To maintain comparability, both detector order and magnification sequence were kept constant for all samples. BSD imaging was used to accentuate compositional contrast, whereas SED imaging was used to capture surface-morphology detail. EDS point spectra and elemental maps were acquired from representative bright regions and from adjacent matrix areas to confirm Fe-rich domains associated with iron oxide and Ca–Si-rich domains associated with wollastonite.

Backscattered (BSD) images at 5000 × were examined using intensity-based segmentation. Bright regions were used as an operational proxy for higher-atomic-number inorganic contrast. EDS, rather than brightness alone, was used for local elemental identification. Numerical descriptor extraction was performed on the single displayed 5000 × BSD field for each selected formulation. Images acquired at other magnifications or using the secondary-electron detector were used for qualitative morphological context.

The image workflow comprised region-of-interest selection, grayscale conversion, mild denoising, percentile-based bright-feature thresholding, speckle removal, and connected-component labeling [60,61]. Area fraction (AF), agglomeration index (AI), and dispersion uniformity index (DUI) were then calculated as local image descriptors [61,62]. These values characterize segmented bright inorganic-contrast features within the analyzed 2D field.

2.8. Multi-response optimization framework

The measured rheological and chemical responses do not necessarily improve in parallel. A formulation may increase stiffness and rutting resistance while reducing strain-controlled damage tolerance. Accordingly, the quantitative multi-response analysis combined (i) desirability normalization with an equal-weight reference baseline, (ii) ranking sensitivity under uncertainty in the response weights, and (iii) Pareto screening of the principal rutting–fatigue trade-off. SEM/EDS observations and AF/AI/DUI descriptors were used only for illustrative mechanistic context and were not inputs to the quantitative ranking.

2.8.1. Desirability normalization and baseline composite score

Each test result was transformed into a dimensionless desirability measure, $d_j \in [0, 1]$, where 0 represents the least desirable outcome and

1 the most desirable. The properties considered were percent recovery R, fatigue life N_f, and complex modulus magnitude $|G^*|$, for which higher values were favored, together with non-recoverable creep compliance J_{nr}, phase angle δ, and selected FTIR indices, for which lower values were preferred. In this baseline framework, the min–max desirability functions were defined as linear first-order transformations of the measured responses. This offers a transparent basis for comparing formulations, but it also implies that the decision value assigned to a given numerical change remains constant across the observed response range. For larger-the-better responses, normalization was performed as

$$d_j = \frac{y_j - y_j^{\min}}{y_j^{\max} - y_j^{\min}} \tag{2}$$

whereas smaller-the-better responses were normalized as

$$d_j = \frac{y_j^{\min} - y_j}{y_j^{\max} - y_j^{\min}} \tag{3}$$

For N_f and $|G^*|$, which spanned wider numerical ranges, logarithmic scaling was applied before normalization so that these variables would not dominate the composite measure. The individual desirability values were then aggregated into an overall baseline composite score using a weighted geometric mean,

$$D = \exp\left(\sum_{j=1}^{m} w_j \ln(d_j)\right), \quad \sum_{j=1}^{m} w_j = 1 \tag{4}$$

2.8.2. Ranking under weight uncertainty

Equal weights were retained only as a transparent reference baseline reflecting the absence of declared response-specific priorities. For the weight-sensitivity analysis, the weight vector was sampled from a symmetric Dirichlet distribution with concentration vector $\alpha = (1, \ldots, 1)$ [63–65]. This distribution has constant density with respect to volume over the feasible simplex, assigns every response the same marginal weight distribution and expected weight, and guarantees non-negative weights summing to one. It was selected as an exchangeable reference scenario. For each of 10,000 draws, desirability and rank were recalculated. Win frequency is the proportion of draws in which a formulation ranked first, and expected rank is its mean rank across draws. Both are conditional sensitivity indices under the selected weight distribution.

For a symmetric Dirichlet model, concentration parameters below one place greater emphasis on sparse or extreme weight combinations, whereas parameters above one increasingly concentrate the sampled weights around equality. The present $\alpha = 1$ analysis lies between these cases and was used to explore the full simplex without assigning different prior distributions to named responses.

2.8.3. Pareto analysis and decision workflow

Pareto dominance was used to map the principal trade-offs in the dataset, most notably the balance between rutting resistance and fatigue response [66]. The decision workflow accordingly moved from desirability normalization to baseline aggregation, then to weight-sensitivity analysis, and finally to Pareto-based verification, as shown in Fig. 4. Pareto screening does not require a prior distribution over response weights, although the resulting non-dominated set still depends on the responses selected for comparison. The purpose was to identify conditional candidates within the tested binder design space.

3. Results and discussion

3.1. Conventional binder properties

The conventional tests show a consistent stiffening effect across the modified binders. Compared with the neat binder, U1, all modified formulations produced higher softening points and lower penetration values (Figs. 5–7), indicating that the combined addition of Fe_2O_3, wollastonite, and MACR shifted the binders toward a more structured state with less tendency to flow, in line with the conventional use of penetration and softening point as descriptors of binder consistency. Softening point increased from 42.95 °C for U1–45.45–52.50 °C for U2-U26, while penetration decreased from 68.60 dmm to 39.88–65.27 dmm. The largest shifts were observed for U6, which reached the highest softening point (52.50 °C, +22.2%), and for U14, which showed the lowest penetration (39.88 dmm, −41.9%). In the sorted bar plots, these relative differences are reported directly as $\Delta SP(\%)$ and $\Delta Pen(\%)$ on each bar, calculated with respect to U1, so that the magnitude of change can be compared visually across formulations. By comparison, U2, U3, U15, and U19 remained closer to the neat binder, indicating that the extent of stiffening was governed strongly by the formulation-processing combination rather than by any simple additive effect.

Penetration and softening point are empirical consistency measures and cannot, by themselves, distinguish physical restructuring from chemical modification. The observed changes are compatible with physical contributions from MACR swelling and uptake of lighter bitumen fractions, rigid-particle reinforcement by Fe_2O_3 and wollastonite, and changes in particle dispersion and colloidal organization [8,13,14,17,21,23]. However, blending was conducted at 155–185 °C for 10–60 min without an inert-gas atmosphere. Oxygen was therefore not excluded. Under these conditions, volatilization and oxidation may occur, while microwave activation may alter the rubber surface through chain scission, partial devulcanization, and changes in oxygen-containing functional groups [11,13,14,18,45,67,68]. Adsorption of polar bitumen fractions on the mineral and oxide surfaces, together with other polar or interfacial interactions, may also affect binder consistency [21,23].

The penetration index followed a different pattern. While the neat binder gave $PI = 1.035$, the modified binders covered a range of $0.376 - 1.068$ (Fig. 8). U2 showed the highest PI, whereas U13 gave the lowest, and several formulations remained below the neat binder despite marked stiffening in both penetration and softening point. This non-monotonic behavior is not surprising, since PI is controlled by the balance between penetration and softening point rather than by either parameter alone. Within this dataset, PI is therefore more appropriately interpreted as a supporting indicator of temperature susceptibility than as a proxy for stiffness. Taken together, the conventional tests point to a consistent increase in the consistency of the unaged binders across the modified formulations. Still, these stiffness-oriented descriptors alone are not sufficient to capture the rheological trade-offs that become apparent later under performance-relevant loading conditions.

Fig. 4. Multi-response optimization workflow of this study.

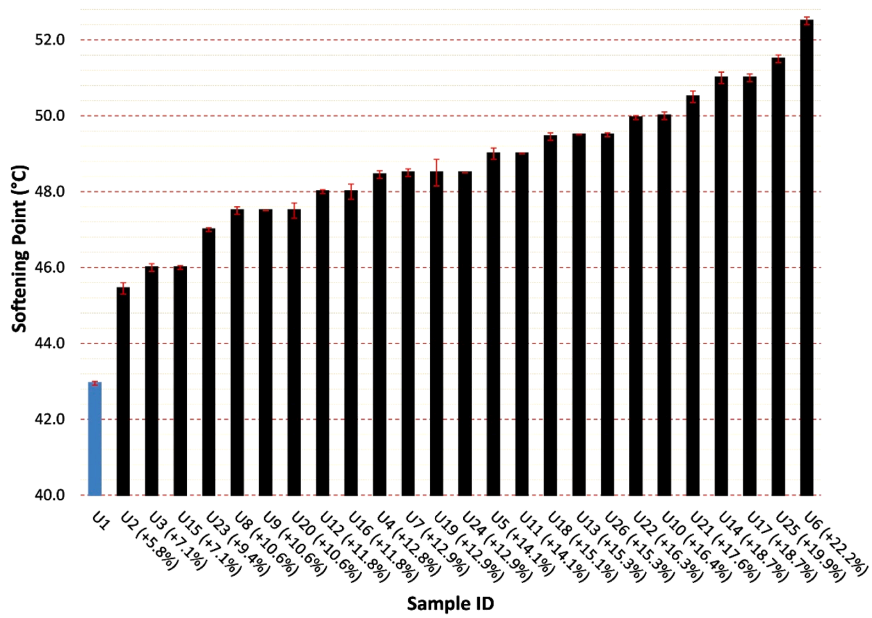

Fig. 5. Softening point of all binders.

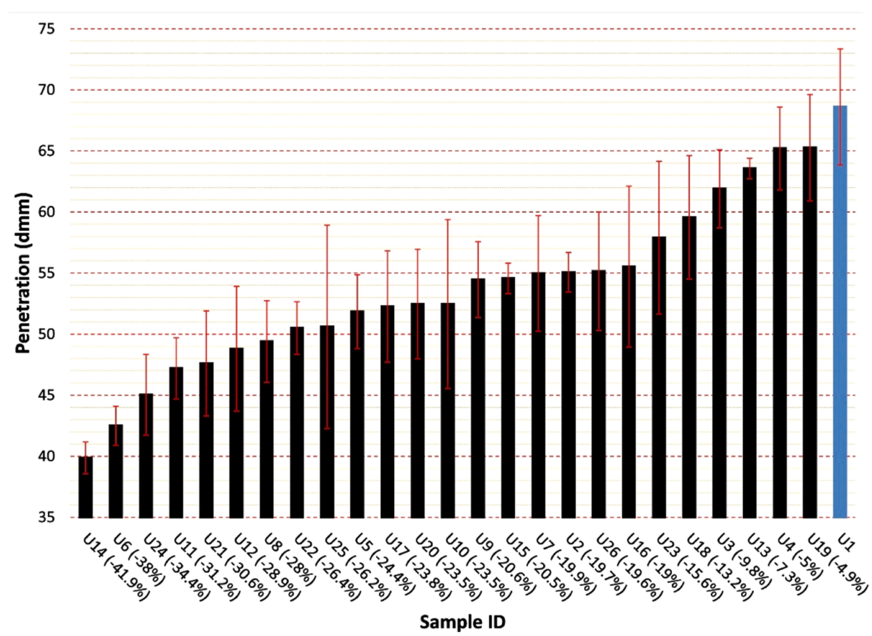

Fig. 6. Penetration of all binders.

3.2. Frequency sweep and MSCR response

3.2.1. Temperature-dependent viscoelastic response

The DSR frequency sweep results show that the multi-additive system changed the viscoelastic response across the tested temperature range of 5–80 °C. Because the subsequent MSCR analysis focuses on rutting resistance, the discussion below emphasizes the response at 60 °C and 10 Hz, however, the lower- and intermediate-temperature data are also relevant for interpreting stiffness development and possible damage sensitivity. In the black diagrams of Fig. 9, most modified binders move toward higher complex shear modulus ($|G^*|$) values than U1 across the measured frequency range, pointing to greater stiffness and reduced deformation susceptibility. This stiffening effect is particularly evident at 60 °C and 10 Hz (Figs. 10–11), in which U1 shows the lowest $|G^*|$ of 3.03 kPa and the highest phase angle (δ) of 86.06°, while many modified binders display both higher modulus and lower phase angle. U26 attains the highest $|G^*|$ (9.10 kPa), whereas U6 pairs a high modulus with one of the lowest phase angles (64.66°), consistent with a more elastic response and reduced viscous dominance at elevated temperature.

Across the design space, $|G^*|$ and δ did not change in perfect parallel. Some formulations reached very high modulus with only limited reductions in phase angle, whereas others showed a stronger elastic shift without producing the highest modulus. This indicates that the additives are not necessarily acting in the same way. MACR appears to drive the main change in viscoelastic balance, while the mineral and oxide phases mainly contribute through filler-like stiffness reinforcement. The behavior is therefore better described as that of a composite material,

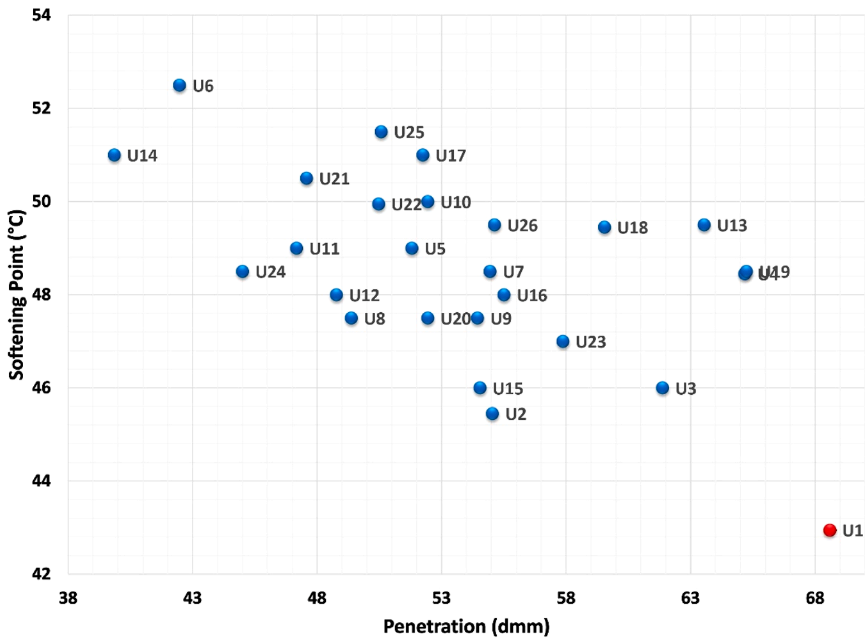

Fig. 7. Penetration versus softening point.

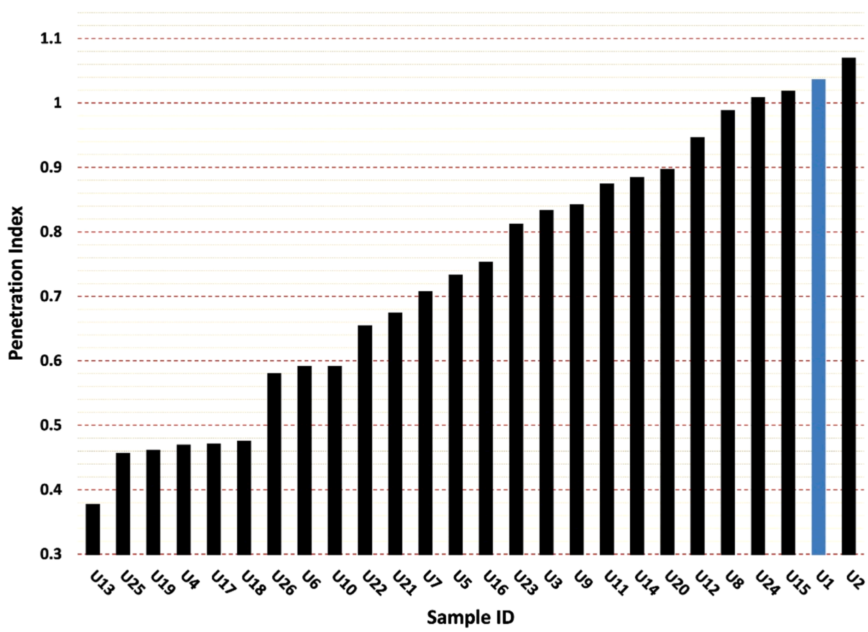

Fig. 8. Penetration index of all binders.

rather than a simple sum of the individual components.

A similar filler-like effect may also influence the response at low and intermediate temperatures, although its engineering implications differ from those observed at high temperature. Under elevated-temperature conditions, increased stiffness together with a lower phase angle is generally favorable for rutting resistance. At low and intermediate temperatures, however, excessive stiffening may reduce the material's ability to accommodate strain and, in turn, compromise damage tolerance. The temperature-dependent frequency-sweep response should therefore be understood as reflecting a trade-off between improved resistance to high-temperature deformation and a possible increase in damage sensitivity under conditions where viscous flow is less dominant.

The pooled Taguchi decomposition provides a descriptive ranking of the assigned main-effect sums of squares (Table 4). MACR accounts for 61.9% of the observed $|G^*|$ variation and 76.3% of the observed phase-angle variation at 60 °C and 10 Hz. Fe_2O_3 and mixing duration contribute 16.8% and 10.0%, respectively, to $|G^*|$, while their phase-angle contributions are smaller. The remaining pooled residual is variation not assigned to these retained main effects and may include interactions, omitted factors, storage/reheating history, and measurement variability.

3.2.2. *Rutting resistance and elastic recovery*

The MSCR results show the same overall trend when rutting behavior is evaluated in a performance-based framework (Fig. 12–14). The neat binder gives the poorest response, with $J_{nr} = 2.41 kPa^{-1}$ and $R_{3.2} = 0\%$, which points to a high susceptibility to permanent deformation and

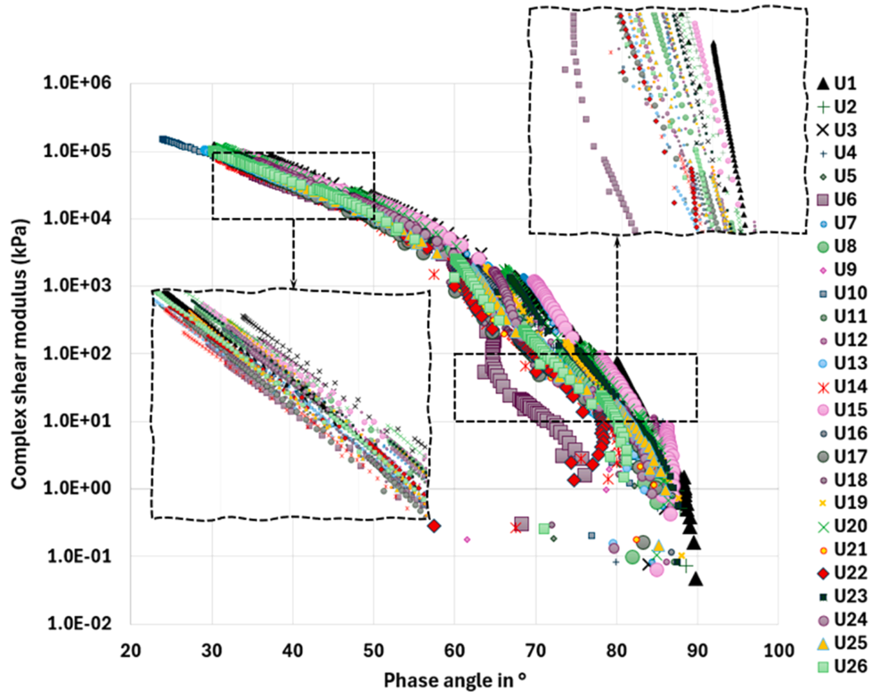

Fig. 9. Black diagram ($|G^*|$ versus δ) for all binders.

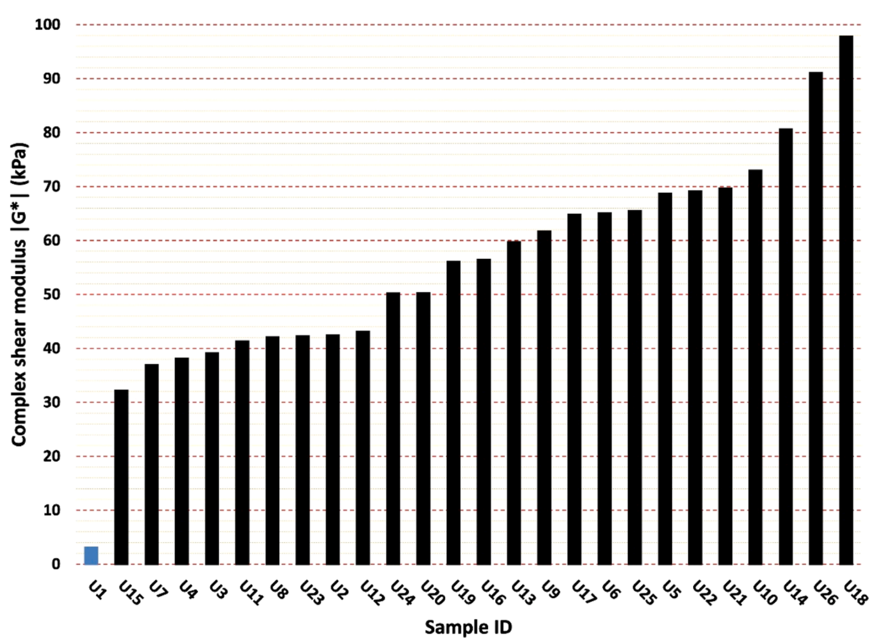

Fig. 10. Complex modulus magnitude $|G^*|$ at 60 °C (10 Hz) for all binders.

virtually no recoverable strain at 60 °C under a 3.2 kPa stress level. Most of the modified binders shift in the expected direction, with lower J_{nr} and higher R values, but the magnitude of that improvement differs markedly across the design space. U6 demonstrates the strongest overall performance in the MSCR dataset, with the lowest J_{nr} (0.49 kPa^{-1}) and the highest recovery (14.78%). U18 and U26 also perform well in terms of J_{nr} (0.50 and 0.56 kPa^{-1}, respectively), while U5 and U10 remain among the better-performing binders in recovery % (5.52% and 5.20%, respectively).

Although MACR clearly improves the MSCR response relative to the neat binder, the recovery values remain lower than those reported for some CR-modified binders at comparable rubber contents [5,55]. One possible explanation is that microwave activation alters part of the rubber network in a way that enhances binder-rubber interaction and dispersion, while at the same time reducing some of the recoverable elastic contribution. On that basis, the main effect of MACR in this dataset is better understood in terms of improved rutting resistance and formulation compatibility, rather than as a route to maximizing elastic recovery.

These results reveal two descriptive patterns. First, the hybrid modification strategy improved the observed rutting-related responses relative to the neat binder. Second, the observed improvement was not shared equally among the modifiers. In the main-effect sums-of-squares decomposition, MACR accounts for 64.6% of the observed $J_{nr,3.2}$ varia-

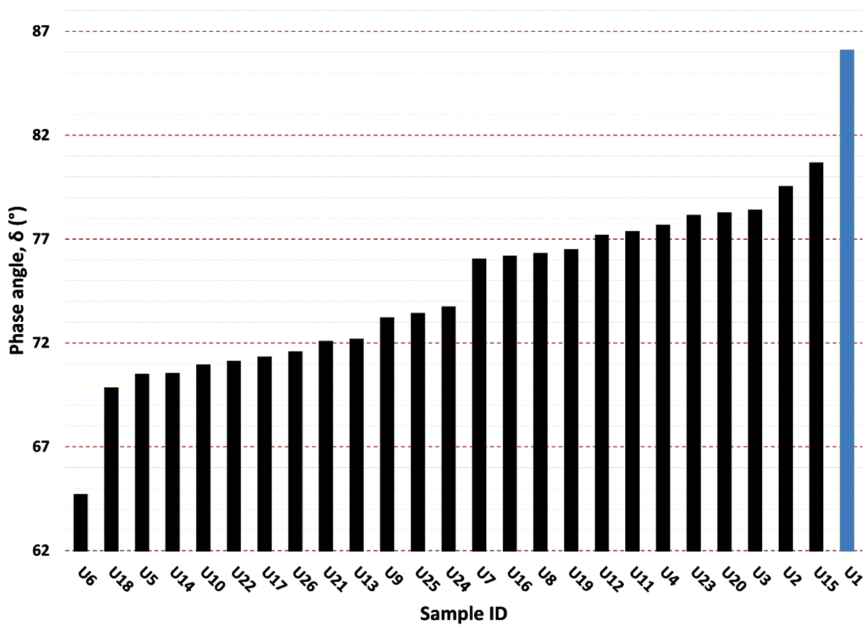

Fig. 11. Phase angle (δ) at 60 °C (10 Hz) for all binders.

Table 4
Descriptive pooled main-effect decomposition for $|G^*|$ and phase angle at 60 °C and 10 Hz.

$\|G^*\|$ at 60 °C, 10 Hz			
Source	**DF**	Assigned main-effect SS	Descriptive share of total SS (%)
MACR	4	4443916606	61.8647
Fe_2O_3	4	1203759291	16.7578
Mixing duration	4	718256250	9.9990
Unassigned pooled residual	12	817356600	11.3776
Total	24	7183288746	100.0000
Phase angle at 60 °C, 10 Hz			
Source	**DF**	Assigned main-effect SS	Descriptive share of total SS (%)
MACR	4	266.6600	76.2539
Fe_2O_3	4	11.6600	3.3343
Mixing duration	4	15.2900	4.3723
Unassigned pooled residual	12	56.0800	16.0395
Total	24	349.7000	100.0000

tion and 70.7% of the observed $R_{3.2}$ variation, whereas the assigned shares of Fe_2O_3 and wollastonite are substantially smaller. The mineral phases may provide secondary reinforcement and restriction of viscous flow, while the recoverable response appears to be governed primarily by the rubber phase within the tested dataset.

The Taguchi stress-sensitivity analysis adds an important qualification. Increasing MACR improves absolute rutting resistance through lower J_{nr} values, but it may also increase stress sensitivity, as indicated by the stress sensitivity parameter ($J_{nr,diff}$) response. In other words, binders with higher MACR contents can show better overall resistance to creep while also responding more nonlinearly as stress increases. A modified binder may therefore perform very well in terms of J_{nr} at a single stress level and still be more stress-dependent than an alternative binder. The modified system strengthens rutting control, but high-temperature behavior cannot be reduced to a single scalar indicator.

3.3. LAS response and rutting–fatigue interaction

The LAS results show why multi-additive binder design cannot be judged from high-temperature stiffness and MSCR alone. Given the preparation sensitivity of LAS-derived fatigue metrics, these results are interpreted comparatively across consistently prepared binders rather than as absolute specification or acceptance values. The damage characteristic curves (Fig. 15) exhibit the expected monotonic reduction in normalized stiffness with increasing damage intensity, but the degree of separation between mix combinations becomes more pronounced at higher damage levels. That divergence points to differences in how rapidly the internal structure degrades under continued loading. While these curves are informative for tracking stiffness retention through the damage process, the fatigue-related summary metrics provide the clearer basis for interpretation.

Fig. 17 presents the geometric-mean LAS fatigue life ($N_{f,geo}$) for all binders. The neat binder, U1, remains the strongest performer in this fatigue summary metric, with $N_{f,geo} \approx 1756$. The modified binders occupy a markedly lower range, from approximately 714 for U26–1310 for U17 (Figs. 16–18 and Table 5). Within the modified set, U17 and U11 are near the upper end of fatigue performance, whereas U26, U20, U13, U7, and U9 cluster toward the lower end. U6 falls in the middle-to-upper part of the modified-binder distribution, with $N_{f,geo} \approx 953$. Selection was not based on fatigue life alone: although U11 has a higher LAS fatigue metric than U6, its poorer rutting-related performance gives a lower overall desirability once all responses are considered under weight uncertainty.

Fig. 16 presents damage intensity at failure (D_f), the relative damage state reached at the LAS-defined failure point.

Fig. 18 compares the calculated LAS fatigue lives at 1.0%, 2.5%, 5.0%, and 15.0% strain. For every binder, N_f decreases sharply as strain increases, while the relative differences among formulations become more consequential at the higher strain levels. Several modified binders perform favorably at low strain. At 15% strain, however, the neat binder, U1, retained the highest LAS life, demonstrating that improved rutting resistance did not translate directly into large-strain damage tolerance.

At 1% strain, several modified binders show higher model-derived LAS lives than U1, consistent with beneficial reinforcement and rubber-mediated load sharing under small deformation. This strain-dependent reversal may have several non-exclusive explanations. Rigid Fe_2O_3/wollastonite inclusions and MACR domains create greater local stiffness contrast, under severe cyclic strain, this heterogeneity

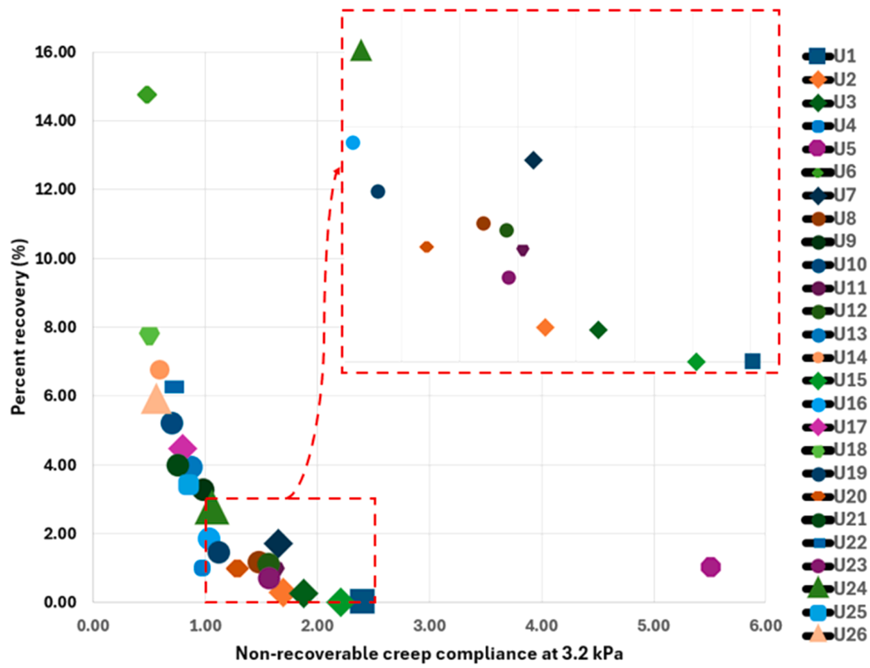

Fig. 12. MSCR results at 60 °C (3.2 kPa), $R_{3.2}$ versus $J_{nr,3.2}$ for all binders.

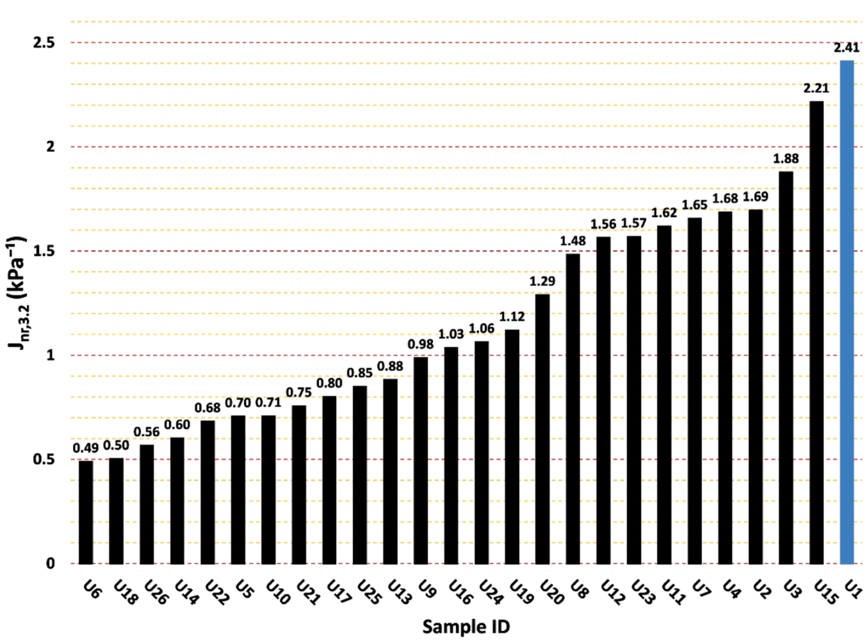

Fig. 13. $J_{nr,3.2}$ at 60 °C (3.2 kPa) for all binders (sorted).

may localize deformation, while any incompletely dispersed domains may act as local stress concentrators. A second, non-exclusive explanation is the sensitivity of the model-derived fatigue life to the fitted LAS/VECD damage relationship and selected failure criterion [57]. U1's higher 15% LAS life is therefore interpreted as greater large-strain tolerance under the adopted LAS criterion.

The neat binder gives $m \approx 4.52$ and $C \approx 6.5 \times 10^5$, while the modified binders span $m \approx 4.47 - 5.12$ and $C \approx 2.8 \times 10^5 - 8.6 \times 10^5$. The relatively limited variation in mmm suggests that many formulations preserve strain sensitivity broadly comparable to that of U1. By contrast, the wider spread in C indicates that formulation and processing mainly shift fatigue capacity upward or downward, depending on how effectively the modifier network forms and disperses. Still, the upper end of the modified range ($m > 5$) shows that some binders become more strain-sensitive, which is consistent with the pronounced drop in life at high strain seen in Fig. 18. Table 5 provides additional context for this reversal. U1 has $m \approx 4.52$ and $C \approx 6.5 \times 10^5$, whereas the modified binders span $m \approx 4.47 - 5.12$ and $C \approx 2.8 \times 10^5 - 8.6 \times 10^5$. Because LAS fatigue life at a prescribed strain is calculated from the fitted strain–life relationship, the combined differences in m and C are amplified at 15% strain, formulations with larger m values are particularly strain-sensitive. U1's high-strain advantage therefore arises from the combined fitted parameters rather than from a directly measured fracture threshold. This sensitivity makes the formulation ranking conditional on the adopted LAS/VECD model and failure criterion [57].

Considered together, Fig. 18 and Table 5 indicate that fatigue

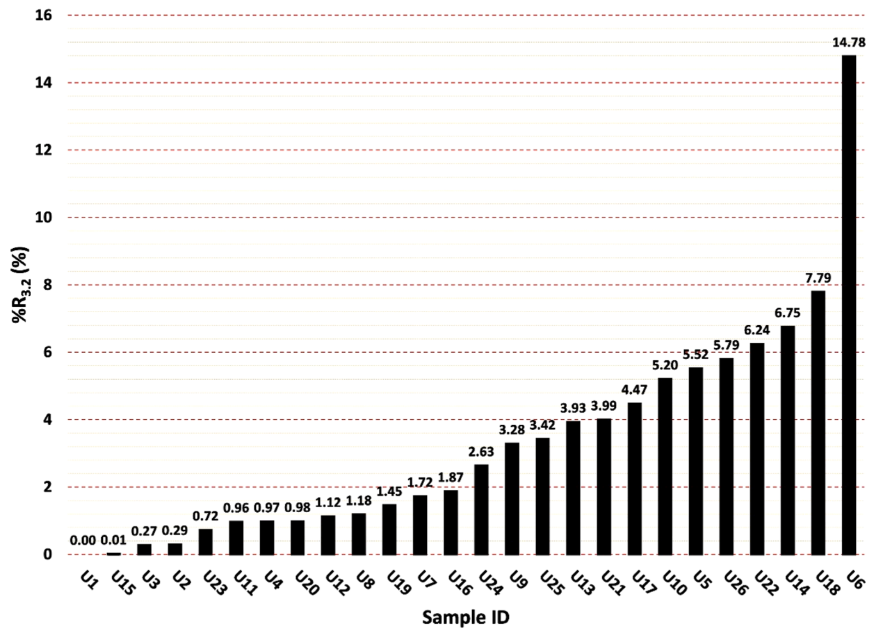

Fig. 14. $R_{3.2}$ at 60 °C (3.2 kPa) for all binders (sorted).

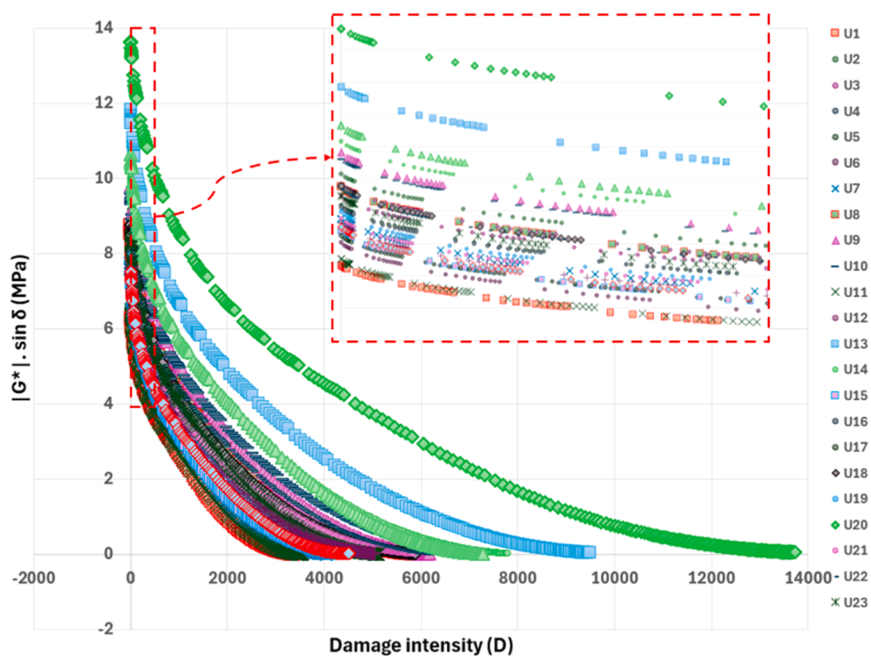

Fig. 15. LAS damage characteristic curves ($|G^*|\sin\delta$ versus D) for all binders.

performance within this design space does not collapse to a single ranking metric. Binders that perform well at low to moderate strain are not always the ones that preserve tolerance under large deformation, so interpreting this trade-off requires attention to both C and m.

At low strain amplitudes, several modified binders perform better than U1, suggesting that a reinforced multiphase structure can enhance endurance under small strains. At 15% strain, the ranking changes sharply. The neat binder performs best, while many of the more structured modified binders fall to very low fatigue lives. Structural reinforcement and elastic-network formation may improve rutting resistance and support fatigue response at moderate strain levels, but under severe deformation the same structural features appear to reduce large-strain tolerance. This interpretation depends on the failure criterion adopted here. Other fatigue criteria may yield different but complementary rankings and should be considered in future sensitivity analyses of modified binders. The LAS results should therefore not be interpreted as a single, strain-independent fatigue ranking. At low strain, several modified binders show model-derived lives comparable to or greater than that of U1, whereas at 15% strain U1 has the highest calculated life. The mineral/oxide and rubber network may support deformation at small or moderate strain but become less tolerant of severe cyclic strain because of local stiffness contrast and strain localization. Incomplete dispersion could intensify this response, but that mechanism cannot be established from the local SEM fields. Moreover, alternative fatigue definitions or failure criteria may produce a different formulation ordering [69]. The present results consequently

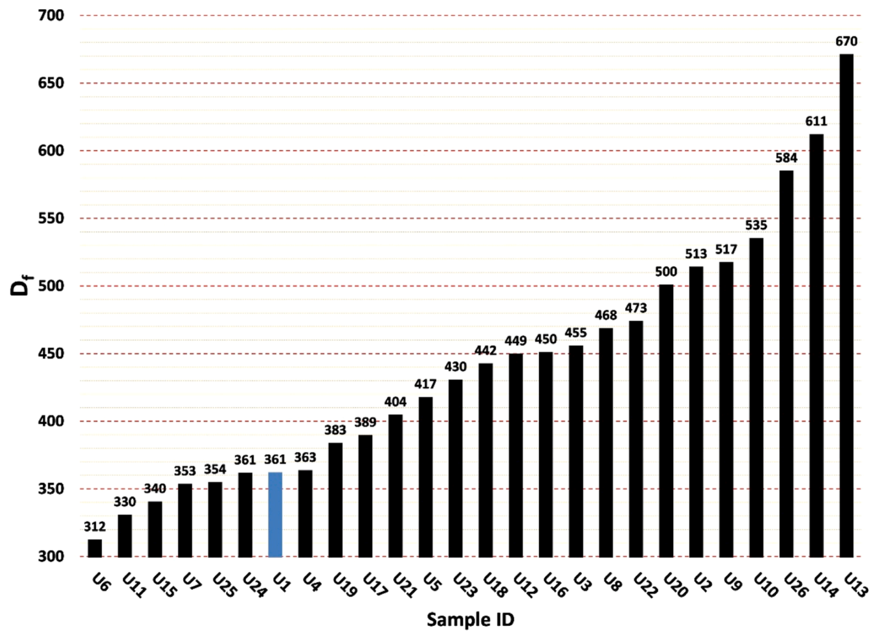

Fig. 16. Damage intensity at failure (D_f) for all binders (sorted).

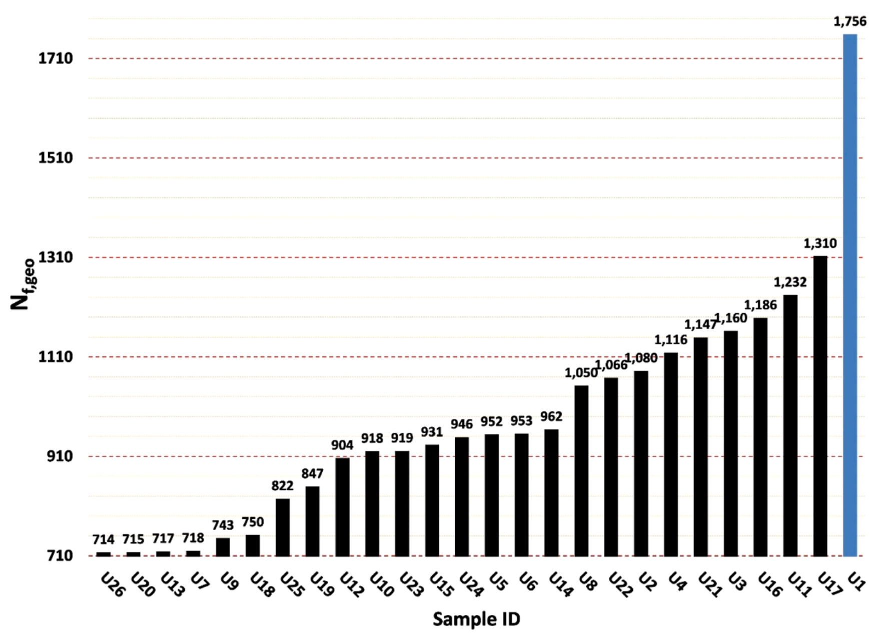

Fig. 17. Geometric-mean fatigue life ($N_{f,geo}$) for all binders (sorted).

demonstrate a strain-dependent LAS response rather than direct evidence of embrittlement.

The pooled main-effect decomposition for $N_{f,geo}$ (Table 6) differs from the high-temperature results. Mixing temperature and rotational speed account descriptively for 32.2% and 29.6% of the observed variation, respectively, while wollastonite accounts for 14.7%, the unassigned residual represents 23.5%. Temperature and shear may jointly affect wetting [67], agglomerate breakup [70], rubber swelling [71], and interfacial organization [68], while uncontrolled storage and reheating histories may also contribute to the unassigned variation.

Fig. 19 confirms that the rutting–fatigue relationship depends on strain level. At 5% strain, some modified binders combine low J_{nr} with mid-to-upper LAS life within the modified group. At 15% strain, the most rut-resistant formulations generally occupy the low-life region. This separation is consistent with a stronger network that restricts creep but may intensify local strain under severe deformation.

3.4. Taguchi screening of governing factors

The Taguchi response tables, and main-effects plots (Fig. 20 and Table 7) summarize the observed factor-level contrasts. MACR produces the strongest monotonic change in J_{nr}, $|G^*|$, and recovery, while Fe_2O_3 and wollastonite act as secondary tuning variables. Because DSR responses were measured once per formulation, the factor-level means, and S/N values are descriptive screening summaries.

Based on results presented in Fig. 20 and Table 7, the pattern is different for the LAS fatigue metric, in which, mixing speed ranks first and mixing temperature second, whereas additive levels are less

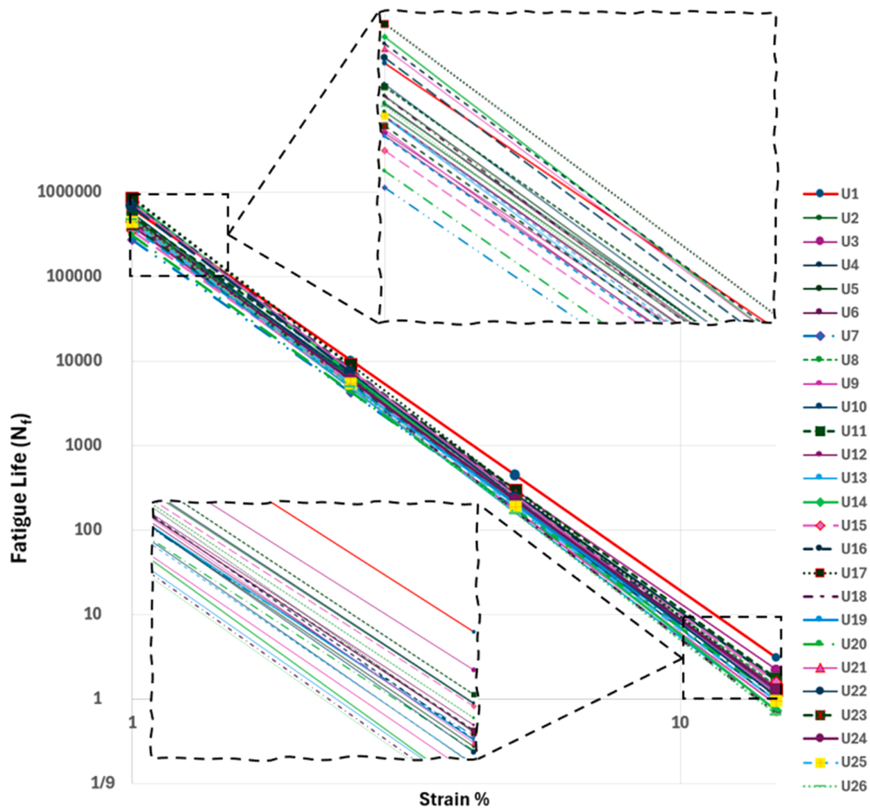

Fig. 18. LAS fatigue life versus strain (log − log).

Table 5
LAS strain–life parameters (*m*, *C*) from LAS regression.

Binder category	Damage exponent (*m*)	Intercept (*C*)
Neat (U1)	~4.52	6.5×10^5
Modified binders (U2–U26)	~4.47–5.12	2.8×10^5 - 8.6×10^5

Table 6
Descriptive pooled main-effect decomposition for $N_{f,geo}$.

Source	DF	Assigned main-effect SS	Descriptive share of total SS (%)
Mixing speed	4	221573	29.6072
Mixing temperature	4	240650	32.1563
Wollastonite	4	109989	14.6970
Unassigned residual	12	176163	23.5395
Total	24	748376	100.0000

decisive. The favorable region is associated with moderate-to-high processing intensity rather than with the maximum level of each additive. In this dataset, fatigue therefore appears to depend more on processing-induced dispersion and phase organization than on material content alone. A similar contrast is evident in the stress-sensitivity response. Higher MACR can strengthen absolute rutting resistance, but it can also intensify nonlinear behavior under elevated stress. The design space is therefore shaped by two distinct mechanisms, one primarily influenced by composition and associated with rutting behavior, and the other primarily influenced by processing and associated with fatigue damage tolerance.

3.5. Chemical and microstructural interpretation

3.5.1. FTIR response

Across all binders, the baseline-corrected FTIR spectra (Fig. 21) retained the expected hydrocarbon-dominated profile of bitumen. No modified formulation exhibited a new dominant band pattern that would indicate extensive formation of a new chemical network. This observation, however, does not demonstrate that modification during blending was entirely physical. Chemical changes occurring at low concentration, within overlapping bitumen bands, or locally at modifier–binder interfaces may not produce a distinct new band. The variations in the carbonyl, sulfoxide, and hydroxyl regions are compatible with differences in oxygenated functionalities and polar or interfacial interactions, but these indices are not reaction-specific and cannot distinguish oxidation from adsorption, modifier contributions, or other interfacial effects [67,68,72].

Figs. 22 and 23 show FTIR indices heatmap and scatter plots of FTIR indices. U1 defines the lower end of the measured oxygenated-index range, whereas U18 and U24 show higher values, principally through their sulfoxide contributions. Because the formulations differed in additive composition, processing conditions, storage duration, and reheating history, these indices should be interpreted as comparative oxygenated signatures rather than direct measurements of reactions occurring during blending. Similarly, the moderate FTIR indices of U6 indicate that it did not possess an unusually strong oxygenated signature at the time of FTIR testing, but they do not establish the absence of limited blending-induced chemistry. Since paired spectra immediately before and after blending were not obtained, the present data cannot quantitatively separate physical restructuring from chemical or interfacial contributions.

3.5.2. SEM, SEM–EDS, and image-based dispersion descriptors

SEM provides local structural context for the FTIR and rheological results. In the displayed BSD fields, U1 is comparatively uniform,

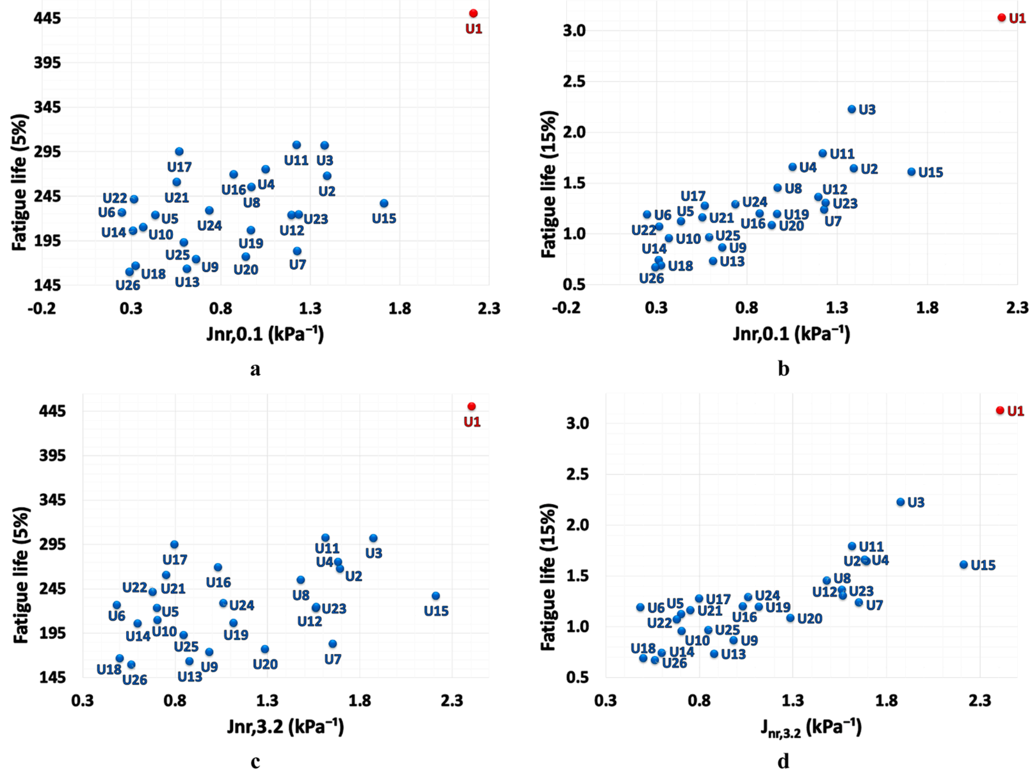

Fig. 19. MSCR–LAS performance maps: (a,b) $J_{nr,0.1}$ versus N_f (5% and 15% strain), (c,d) $J_{nr,3.2}$ versus N_f (5% and 15% strain).

whereas selected modified binders contain bright inorganic-contrast features (Fig. 24). The representative U6 field contains a finer-appearing bright-feature population than the shown U14 and U18 fields. This visual pattern is consistent with, but does not prove, better local breakup under the U6 thermal-shear condition.

Local SEM–EDS spectra support the assignment of selected bright regions to Fe-rich and Ca–Si-rich inorganic domains. U1 showed no added Fe, Si, or Ca in the sampled region, whereas the selected modified fields contained formulation-dependent local signals.

AF, AI, and DUI were calculated from 5000 × BSD field for each of the 26 binders, comprising the neat binder U1 and the 25 modified binders U2–U26. Fig. 25 presents selected image and segmentation examples only, illustrating the calculation of these descriptors and the range of local morphologies observed across the complete sample set. Within the displayed examples, U2 and U8 exhibit lower AI and higher DUI than U13 and U18, indicating a finer local bright-feature size distribution in the particular analyzed fields. U1 illustrates why AI should not be interpreted as a modifier-dosage metric: despite its low bright-phase area fraction, its analyzed field is dominated by one detected feature. Although descriptors were obtained for all 26 binders, each value characterizes only one local 2D field and therefore does not constitute a statistically estimate of bulk dispersion. The descriptors were not included in the desirability, Pareto, weight-uncertainty, or Taguchi rankings. Consequently, they suggest formulation- and processing-dependent differences in local phase organization but cannot establish that one formulation is more uniformly dispersed throughout the bulk binder.

3.5.3. *Microstructure–property interpretation*

Taken together, the rheological results establish a formulation-and processing-dependent performance response, FTIR constrains but does not eliminate possible chemical contributions, and SEM/EDS supplies illustrative local context. A plausible interpretation is that MACR governs much of the high-temperature viscoelastic response while the mineral/oxide phases provide secondary reinforcement.

3.6. *Multi-response optimization and selection of optimal formulation*

3.6.1. *Baseline composite ranking*

No single response captures the complete material trade-off. In the equal-weight baseline (Table 8), U6 ranks first ($D = 0.6869$), followed by U14 (0.6790), U21 (0.6612), and U17 (0.6324). Equal weighting is used as a transparent reference benchmark rather than as a claim about field priorities. Because the weighted geometric mean penalizes very poor normalized responses, the leading formulations have comparatively balanced measured profiles rather than maximizing every criterion. The resulting ordering remains conditional on the included responses, normalization functions, and equal-weight assumption.

The Taguchi main-effects analysis of composite desirability (Fig. 26) identifies the factor-level combination corresponding to U6 as the leading equal-weight screening condition. Mixing temperature produces the largest observed factor-level contrast, followed by MACR, wollastonite, duration, speed, and Fe_2O_3. These are descriptive contrasts within the tested factor levels and equal-weight decision model.

3.6.2. *Ranking under weight uncertainty and Pareto validation*

The baseline ranking was recalculated for 10,000 wt vectors sampled from the feasible simplex using the symmetric Dirichlet reference scenario described in Section 2.8.2. (Table 9) Under this scenario, U6 has the highest win frequency (0.4050), whereas U14 has the slightly better expected rank (2.7364 compared with 2.8666 for U6). U17 and U21 form the next tier. These values quantify ranking sensitivity to weights under the specified distribution. They are conditional on the Dirichlet concentration vector, included responses, normalization functions, and candidate set.

Pareto analysis in the rutting–fatigue plane (Fig. 27) serves as an external check on whether the leading candidates emerge only because the multi-response procedure reduces several metrics to a single scalar index. As shown in Fig. 27, U6, U14, U17, and U21 fall on the non-dominated boundary, so no other formulation achieves both a lower $J_{nr,3.2}$ and a higher LAS N_f at 2.5% strain at the same time. U22 also

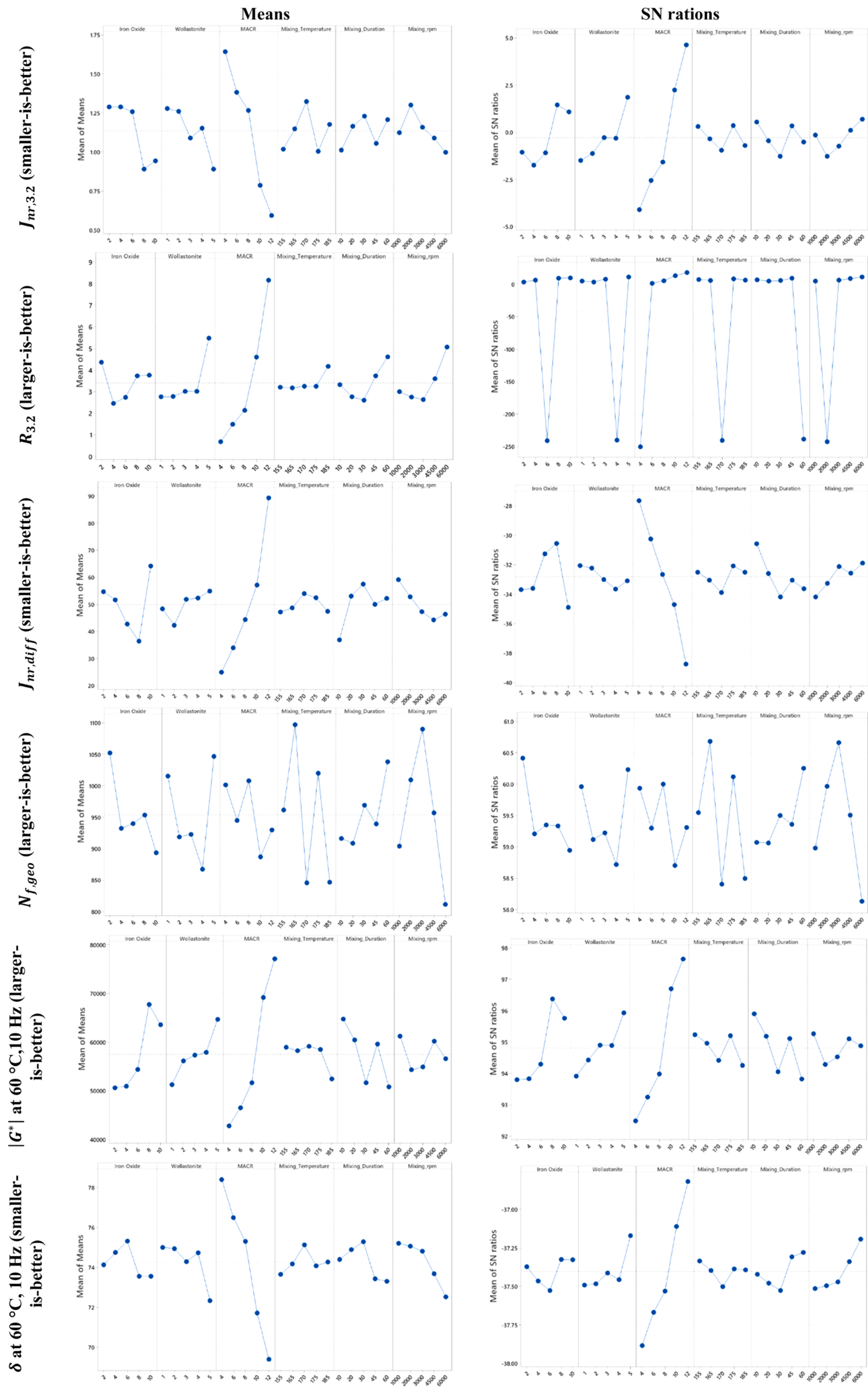

Fig. 20. Main-effects plots (means and S/N ratios) for key responses.

appears as non-dominated in this two-objective view, but its poor ranking once the full response set is taken into account makes the limitation of that projection clear, two-objective non-dominance is necessary, but not sufficient, for overall robustness. The Pareto check therefore supports the shortlist obtained from the weight-uncertainty ranking, while the final selection is still based on the full multi-response framework.

3.6.3. Mechanistic basis of U6

U6 is the leading screening candidate because it combines the lowest $J_{nr,3.2}$ (0.49 kPa^{-1}), the highest $R_{3.2}$ (14.78%), mid-to-upper modified-binder LAS life ($N_{f,geo} \approx 953$), and the highest equal-weight desirability (0.6869). Its moderate FTIR indices do not indicate an unusually strong oxygenated signature. U6 was selected by the quantitative multi-response decision model, not by AF, AI, DUI, or visual SEM

Table 7
Taguchi response tables (means and S/N ratios) for key responses.

$J_{nr,3.2}$ (kPa,$^{-1}$, smaller is better)							
Factor / statistic	**Level 1**	**Level 2**	**Level 3**	**Level 4**	**Level 5**	**Delta**	**Rank**
S/N ratio (dB)							
Fe_2O_3	−1.0522	−1.7581	−1.0993	1.4543	1.0698	3.2124	3
Wollastonite	−1.5014	−1.1276	−0.2853	−0.3158	1.8446	3.346	2
MACR	−4.1023	−2.5648	−1.5837	2.2445	4.6208	8.723	1
Temperature	0.3022	−0.3583	−0.9628	0.3478	−0.7143	1.3107	6
Duration	0.5451	−0.4607	−1.2843	0.3367	−0.5222	1.8294	5
Speed	−0.1514	−1.2853	−0.7453	0.1021	0.6945	1.9798	4
Mean response							
Fe_2O_3	1.2888	1.2883	1.2575	0.8914	0.9437	0.3974	2
Wollastonite	1.2774	1.2605	1.0894	1.1515	0.8909	0.3865	3
MACR	1.6415	1.3822	1.2656	0.7862	0.5943	1.0472	1
Temperature	1.0186	1.1474	1.3233	1.0031	1.1773	0.3201	4
Duration	1.0119	1.165	1.2294	1.0555	1.208	0.2175	6
Speed	1.1249	1.3016	1.1576	1.0886	0.997	0.3045	5
$R_{3.2}$ (%, larger is better)							
Factor / statistic	**Level 1**	**Level 2**	**Level 3**	**Level 4**	**Level 5**	**Delta**	**Rank**
S/N ratio (dB)							
Fe_2O_3	3.196	6.092	−241.0	9.179	9.477	250.498	4
Wollastonite	4.793	3.396	7.656	−240.1	11.15	251.229	3
MACR	−250.1	1.402	4.975	13.06	17.61	267.724	1
Temperature	7.191	5.725	−240.5	8.17	6.331	248.664	5
Duration	6.719	4.502	5.394	9.062	−238.8	247.817	6
Speed	4.483	−242.6	5.925	8.345	10.78	253.396	2
Mean response							
Fe_2O_3	4.3656	2.4687	2.7334	3.7355	3.76	1.8969	5
Wollastonite	2.769	2.7768	3.0168	3.0222	5.4782	2.7092	2
MACR	0.6859	1.4929	2.1369	4.5962	8.1511	7.4652	1
Temperature	3.2077	3.175	3.2535	3.2514	4.1755	1.0005	6
Duration	3.3297	2.7674	2.6147	3.7403	4.6109	1.9962	4
Speed	2.9984	2.7572	2.6448	3.6032	5.0595	2.4147	3
$J_{nr,diff}$ (%, smaller is better)							
Factor / statistic	**Level 1**	**Level 2**	**Level 3**	**Level 4**	**Level 5**	**Delta**	**Rank**
S/N ratio (dB)							
Fe_2O_3	−33.71	−33.63	−31.28	−30.58	−34.90	4.32	2
Wollastonite	−32.07	−32.25	−33.01	−33.66	−33.11	1.58	6
MACR	−27.68	−30.27	−32.68	−34.72	−38.75	11.07	1
Temperature	−32.52	−33.06	−33.90	−32.09	−32.53	1.82	5
Duration	−30.58	−32.60	−34.21	−33.07	−33.64	3.63	3
Speed	−34.19	−33.28	−32.13	−32.59	−31.91	2.28	4
Mean response							
Fe_2O_3	54.67	51.66	42.73	36.41	64.16	27.75	2
Wollastonite	48.29	42.31	51.83	52.31	54.88	12.57	5
MACR	25.00	33.92	44.35	57.16	89.20	64.2	1
Temperature	47.21	48.65	53.93	52.45	47.38	6.73	6
Duration	36.94	53.06	57.47	50.02	52.15	20.53	3
Speed	59.04	52.79	47.25	44.24	46.32	14.8	4
$N_{f,geo}$ (larger is better)							
Factor / statistic	**Level 1**	**Level 2**	**Level 3**	**Level 4**	**Level 5**	**Delta**	**Rank**
S/N ratio (dB)							
Fe_2O_3	60.41	59.21	59.35	59.33	58.94	1.47	4
Wollastonite	59.96	59.11	59.22	58.72	60.23	1.51	3
MACR	59.93	59.30	60.00	58.70	59.31	1.29	5
Temperature	59.55	60.68	58.40	60.12	58.50	2.28	2
Duration	59.07	59.06	59.50	59.36	60.25	1.19	6
Speed	58.98	59.97	60.66	59.50	58.13	2.53	1
Mean response							
Fe_2O_3	1052	932.1	939.8	953.6	893.5	158.5	4
Wollastonite	1015.3	918.9	922.8	867.5	1046.4	178.9	3
MACR	1001.5	944.9	1007.8	887.1	929.6	120.7	6
Temperature	961.4	1097.2	845.7	1019.9	846.8	251.5	2
Duration	916.1	908.6	969.0	939.3	1037.9	129.3	5
Speed	904.1	1009.2	1089.6	956.7	811.3	278.4	1
$\|G^*\|$ at 60 °C, 10 Hz (Pa, larger is better)							
Factor / statistic	**Level 1**	**Level 2**	**Level 3**	**Level 4**	**Level 5**	**Delta**	**Rank**
S/N ratio (dB)							
Fe_2O_3	93.79	93.83	94.29	96.37	95.76	2.58	2
Wollastonite	93.91	94.42	94.90	94.89	95.92	2.01	4
MACR	92.49	93.24	93.98	96.69	97.64	5.15	1
Temperature	95.23	94.96	94.41	95.20	94.25	0.99	5
Duration	95.89	95.18	94.05	95.11	93.82	2.08	3
Speed	95.26	94.28	94.52	95.11	94.88	0.98	6
Mean response							
Fe_2O_3	50624	50922	54354	67673	63570	17049	2

(continued on next page)

Table 7 (*continued*)

$J_{nr,3.2}$ (kPa,$^{-1}$, smaller is better)							
Wollastonite	51233	56128	57276	57860	64645	13413	4
MACR	42789	46533	51632	69140	77049	34261	1
Temperature	58941	58206	59151	58441	52404	6747	6
Duration	64705	60402	51653	59579	50804	13900	3
Speed	61221	54295	54866	60168	56594	6926	5
Phase angle (δ) at 60 °C, 10 Hz (°, smaller is better)							
Factor / statistic	**Level 1**	**Level 2**	**Level 3**	**Level 4**	**Level 5**	**Delta**	**Rank**
S/N ratio (dB)							
Fe_2O_3	−37.37	−37.47	−37.53	−37.32	−37.33	0.2	5
Wollastonite	−37.49	−37.48	−37.41	−37.46	−37.17	0.32	2
MACR	−37.88	−37.67	−37.53	−37.11	−36.82	1.06	1
Temperature	−37.34	−37.40	−37.50	−37.39	−37.39	0.17	6
Duration	−37.42	−37.48	−37.53	−37.31	−37.28	0.25	4
Speed	−37.51	−37.50	−37.47	−37.34	−37.19	0.32	3
Mean response							
Fe_2O_3	74.12	74.73	75.31	73.56	73.56	1.75	5
Wollastonite	75.00	74.93	74.29	74.72	72.34	2.66	3
MACR	78.40	76.48	75.29	71.71	69.39	9.01	1
Temperature	73.65	74.17	75.12	74.08	74.26	1.47	6
Duration	74.39	74.88	75.28	73.42	73.30	1.98	4
Speed	75.20	75.05	74.81	73.68	72.53	2.68	2

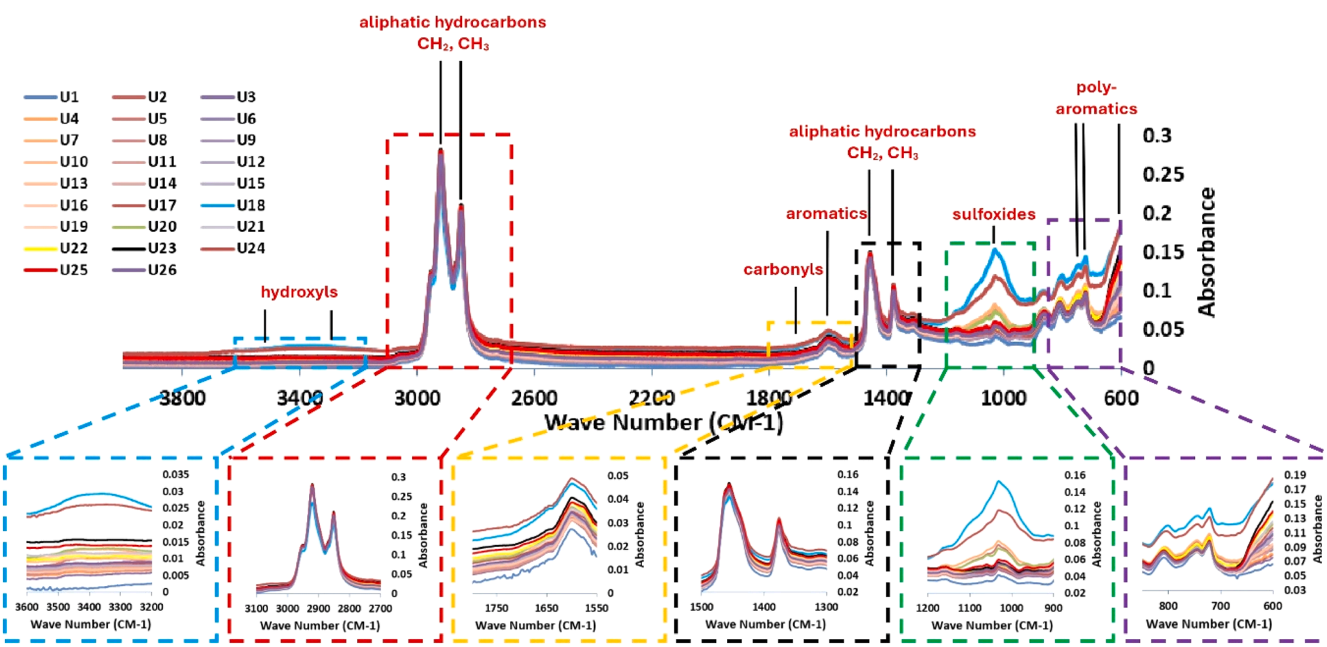

Fig. 21. Baseline-corrected FTIR spectra of all binders.

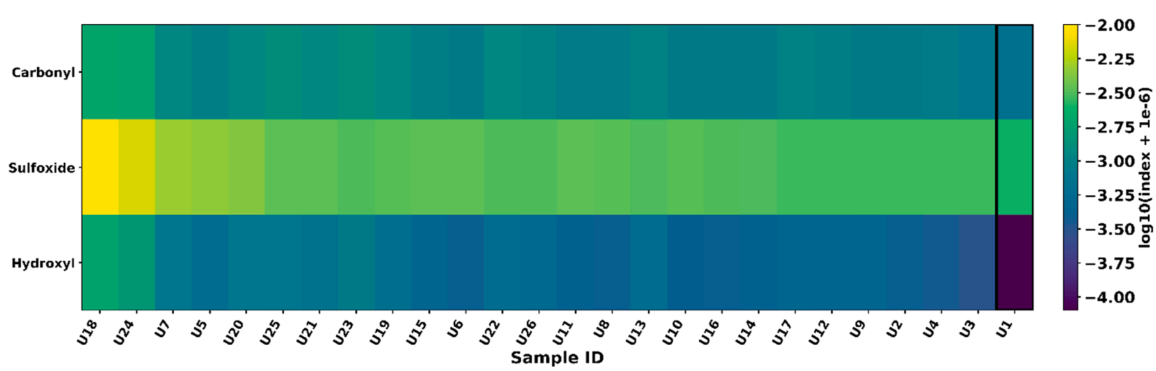

Fig. 22. FTIR indices heatmap ($\log_{10}$ scale) sorted by OI=CI + SI.

interpretation.

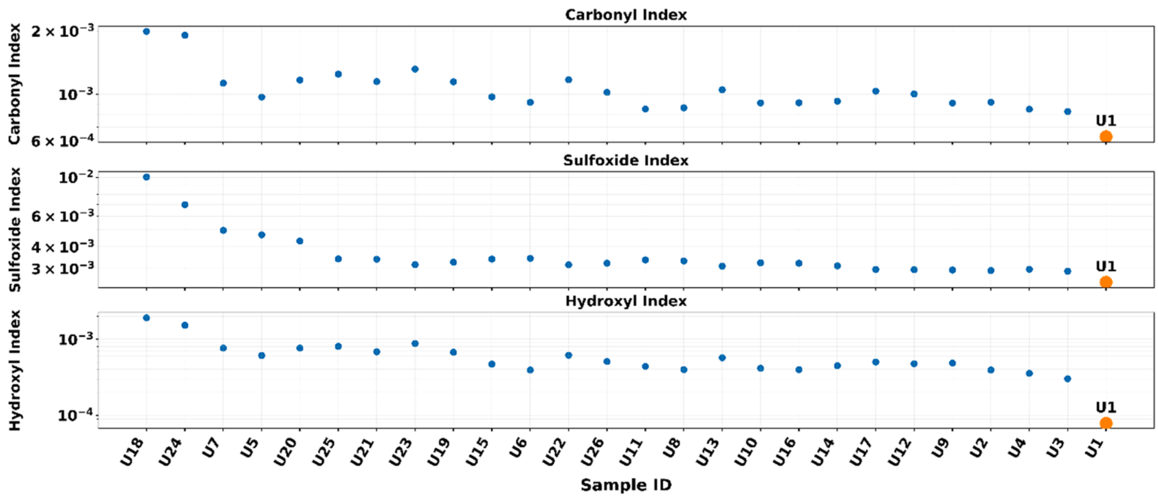

Fig. 23. Small-multiple scatter plots of carbonyl, sulfoxide, and hydroxyl (sorted by OI=CI+SI).

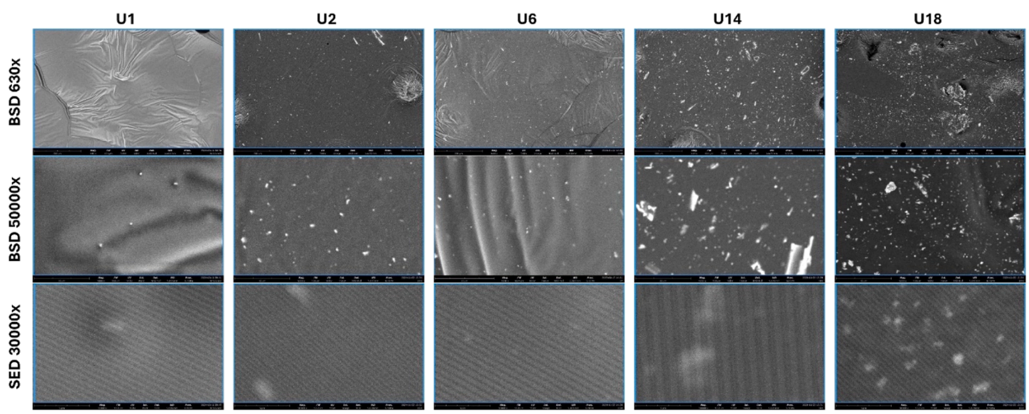

Fig. 24. SEM micrographs for neat binder U1 and selected modified binders U2, U6, U14, and U18 (BSD 630 ×/5000 ×, SED 30,000 ×).

3.6.4. Decision stability

Decision stability was examined using two computational perturbations: resampling of the simulated weight vectors and leave-one-candidate-out recalculation. These analyses evaluate numerical stability of the decision procedure, they do not remove dependence on the Dirichlet prior, normalization choices, candidate set and included responses.

Fig. 28 shows bootstrap win-frequency distributions for leading formulations. Across $B = 1000$ bootstrap replicates, the simulated weight scenarios were resampled with replacement and the rankings were recomputed (Table 10). U6 remained the most frequent winner, with mean win frequency 0.4172 ± 0.0070, followed by U14 (0.2713 ± 0.0063). U17 and U21 formed a third tier and were nearly indistinguishable under resampling. These bootstrap results measure the numerical stability of the estimated win frequencies for weight vectors generated from Dirichlet. Because the bootstrap resamples scenarios generated from the same prior distribution, it does not evaluate robustness to alternative Dirichlet concentration parameters and should not be interpreted as representing uncertainty arising from different experimental settings.

In each LOO iteration (Table 11), one formulation was removed, the robust ranking was recomputed for the remaining candidates, and both the winner and the top 4 set were recorded. Across the 25 iterations, U6 remained the top formulation in 23 cases, while U14 was selected in the other 2, no other formulation reached rank−1. The top-tier set was, on the whole, largely unchanged, which indicates that the decision is not materially affected by small changes in the available alternatives.

Taken together, the bootstrap and leave-one-out analyses show that U6 remains the most frequent leading candidate within the stated decision model and Dirichlet weight scenario. This is evidence of computational ranking stability under those assumptions, not evidence field-performance probability, or universal multi-criteria dominance.

4. Further discussions and interpretation of results

4.1. Integrated interpretation of multi-additive modification

The main finding of this study is that the hybrid Fe_2O_3-wollastonite-MACR system does not exhibit additive behavior in any simple or direct way. When the three modifiers are introduced under different thermal-shear histories, the response space is shaped less by isolated one-factor effects than by interaction, competition, and sensitivity to processing conditions. In that sense, the Taguchi design was not simply an efficient choice. The measured responses make clear that nominal formulation and actual processing cannot be treated as separate without stripping the system of its physical meaning.

The conventional tests indicate a clear tendency toward greater unaged consistency, yet the rheological results show why that characterization on its own is insufficient. Across the design space, stiffness improvement, rutting resistance, recoverability, and fatigue-related damage tolerance do not evolve in parallel. Some formulations markedly reduce non-recoverable deformation but provide only moderate recovery or limited tolerance under large-strain fatigue loading. Others retain more favorable fatigue behavior while offering less protection

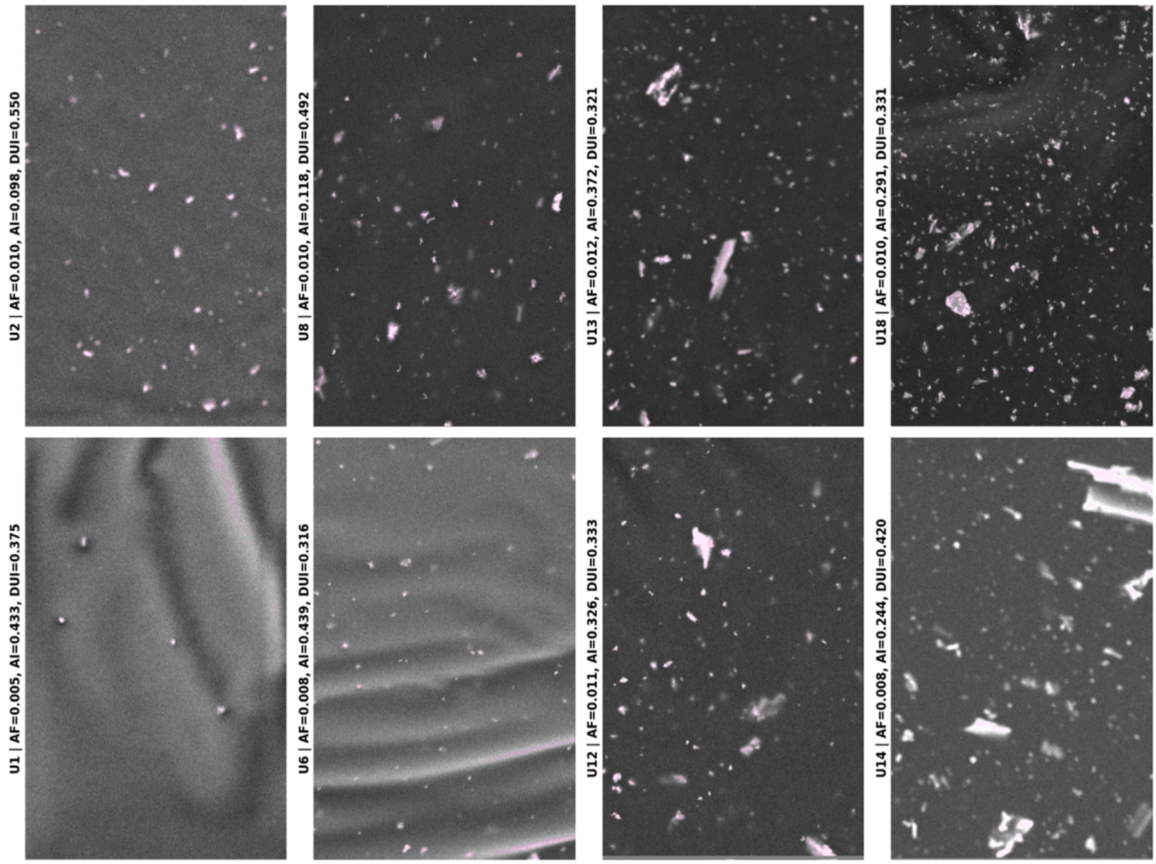

Fig. 25. BSD ROIs (5000 ×) and bright-phase segmentation overlays for selected binders with AF, AI, and DUI shown.

Table 8
Baseline composite desirability ranking of formulations.

Rank	Sample	Composite desirability *D*	Rank	Sample	Composite desirability *D*
1	U6	0.6869	14	U23	0.3628
2	U14	0.6790	15	U20	0.3282
3	U21	0.6612	16	U3	0.3131
4	U17	0.6324	17	U4	0.2591
5	U5	0.6063	18	U22	0.0804
6	U10	0.5646	19	U26	0.0660
7	U16	0.5592	20	U19	0.0531
8	U11	0.5063	21	U2	0.0510
9	U25	0.4857	22	U7	0.0481
10	U8	0.4847	23	U13	0.0480
11	U9	0.4672	24	U18	0.0008
12	U12	0.4565	25	U15	0.0001
13	U24	0.4072			

against rutting. This divergence is not a secondary feature of the system. It is its defining material characteristic.

The binder is therefore best understood as a processing-dependent multi-phase composite. Iron oxide and wollastonite function primarily as rigid reinforcing phases that restrain viscous flow and contribute to high-temperature stiffness. MACR serves as the main elasticity-enabling phase and the dominant contributor to MSCR response and high-temperature viscoelastic behavior. Fatigue-related performance, however, depends more strongly on whether these phases are brought together into a cooperative microstructure or left in a heterogeneous, cluster-prone arrangement. This helps explain why mixing temperature and shear intensity emerge so clearly in the LAS-related screening results. They determine whether the additives are simply present in the blend or are effectively integrated into the material structure.

4.2. Distinct controls for rutting resistance and damage tolerance

Across the formulation space examined here, the results are consistent with the established distinction between rutting response and strain-controlled damage tolerance. Rutting resistance is controlled chiefly by the modifier package, with MACR playing the dominant role and the mineral and oxide phases contributing a secondary reinforcing effect. By contrast, fatigue-related behavior is driven more strongly by processing conditions, especially mixing temperature and mixing rpm. The contribution of this study, then, does not lie in establishing the rutting-fatigue distinction as such, but in showing how that distinction emerges within the Fe_2O_3-wollastonite-MACR system under the Taguchi design examined here. In a hybrid binder system of this type, fatigue tolerance therefore cannot be inferred from rutting indicators, and the reverse is equally true.

This separation also helps clarify the behavior of formulations that perform very well in MSCR but not in high-strain LAS. The same structural reinforcement and network development that suppress non-recoverable creep may, when dispersion is still incomplete, introduce local stiffness mismatch and promote strain localization. A binder that is softer, or simply less strongly reinforced, may show better tolerance under large strain while still failing to provide sufficient rutting resistance. The formulation problem is thus unavoidably multi-objective.

4.3. Role of the mineral/oxide phases

The results indicate that the mineral/oxide additives play a supporting rather than dominant role. Their most consistent effect is to increase binder consistency and limit flow within the bitumen-rich matrix. In practical terms, they shift the system toward lower J_{nr} and higher $|G^*|$, although the magnitude of this effect depends on the quality of dispersion and remains subordinate to the contribution of MACR in

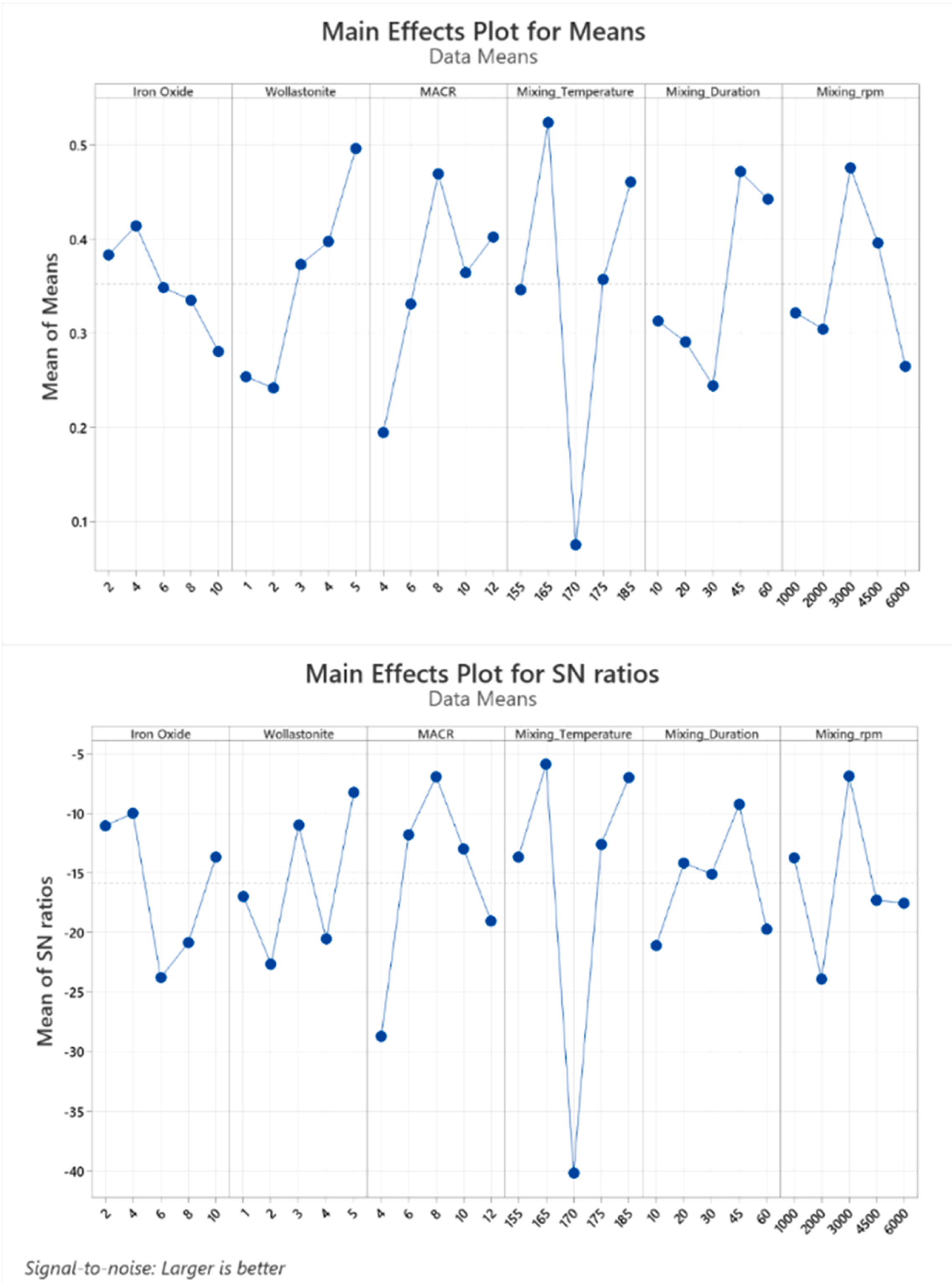

Fig. 26. Main-effects plots for mean composite desirability *D* (mean and S/N, larger-is-better).

the key high-temperature performance measures. Within this binder system, Fe_2O_3 and wollastonite do not by themselves resolve the observed mismatch between improved rutting-related indicators and strain-controlled damage tolerance. Their role is better understood as one of reinforcement, since the value they offer depends on how effectively they are distributed and how they work with the rubber-supported structure.

4.4. *Processing as a design variable*

Processing should therefore be regarded as a primary design variable, not merely as a laboratory setting. The optimum identified here cannot be reduced to composition alone because it reflects a coupled composition and processing state. Increasing temperature, extending mixing time, or applying stronger shear does not automatically improve

Table 9
Multi-response ranking under weight uncertainty (*WF*, *ER*, Pareto).

Rank	Sample	Win Freq	Exp Rank	Pareto	Rank	Sample	Win Freq	Exp Rank	Pareto
1	U6	0.4050	2.8666	TRUE	14	U23	0.0000	14.7360	FALSE
2	U14	0.2734	2.7364	TRUE	15	U20	0.0000	15.8142	FALSE
3	U17	0.1496	4.1080	TRUE	16	U3	0.0000	16.1310	FALSE
4	U21	0.1480	2.8736	TRUE	17	U4	0.0000	17.1296	FALSE
5	U11	0.0116	8.5584	FALSE	18	U22	0.0000	18.0140	TRUE
6	U16	0.0110	6.5486	FALSE	19	U26	0.0000	19.2776	FALSE
7	U8	0.0004	9.7542	FALSE	20	U13	0.0000	20.2502	FALSE
8	U12	0.0004	11.3446	FALSE	21	U2	0.0000	20.2984	FALSE
9	U5	0.0002	5.0974	FALSE	22	U19	0.0000	20.3436	FALSE
10	U9	0.0002	10.6086	FALSE	23	U7	0.0000	20.5854	FALSE
11	U24	0.0002	12.8818	FALSE	24	U18	0.0000	23.6156	FALSE
12	U10	0.0000	7.1538	FALSE	25	U15	0.0000	24.2736	FALSE
13	U25	0.0000	9.9988	FALSE					

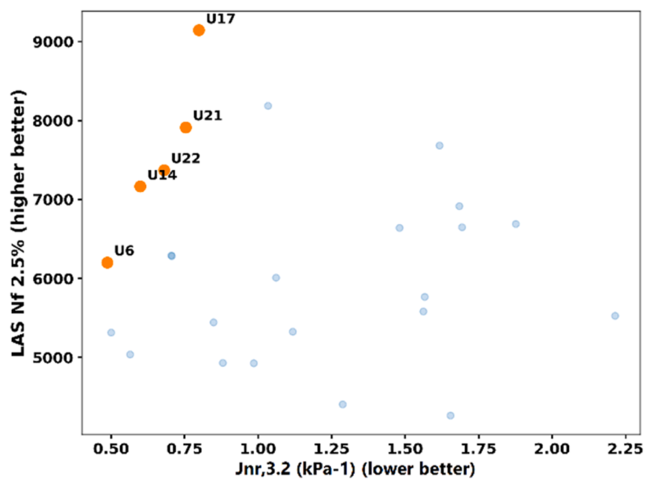

Fig. 27. Pareto front of rutting–fatigue performance ($J_{nr,3.2}$ versus LAS N_f at 2.5% strain).

performance, but these parameters define the range over which dispersion, wetting, swelling, and interfacial development can evolve toward a more coherent internal structure. Temperature determines the accessible microstructural window, duration provides the time needed for that structure to form, and shear controls the fineness and uniformity with which the phases are distributed.

4.5. Implications for formulation screening and study scope

These results support the feasibility-first decision framework adopted in this study. A formulation must remain acceptable across the principal measured response categories before compromise-based ranking becomes meaningful. On that basis, U6 emerged as the leading conditional compromise under the equal-weight baseline and uniform-simplex Dirichlet sensitivity scenario. This result does not establish that U6 outperforms every formulation on every response

This exploratory study is limited to laboratory-prepared binders that were not aged using a standardized RTFOT or PAV protocol. This exploratory study is limited to laboratory-prepared, nominally unaged binders. The DSR responses were single measurements, so within-formulation standard deviations and replicate-based significance tests are unavailable. The 25 formulations were prepared over approximately two weeks, stored in separate uncovered vessels at ambient room conditions, and reheated as required for sequential test programs. These conditions may permit surface oxidation, physical hardening, settling, or thermal-history effects. Finally, the L25 array screens main effects but cannot resolve all interactions, and the multi-response result is conditional on the included responses, normalization, and uniform-simplex weight model. Replicated DSR testing, controlled sealed storage, documented reheating, aging protocols, viscosity/workability testing, and asphalt-mixture validation are required before specification or field recommendations.

SEM descriptors were derived from one displayed 2D field for each selected formulation. The fields were not statistically randomized or replicated for quantitative analysis, therefore, AF, AI, and DUI cannot be generalized to bulk-binder dispersion. The descriptors were not used in

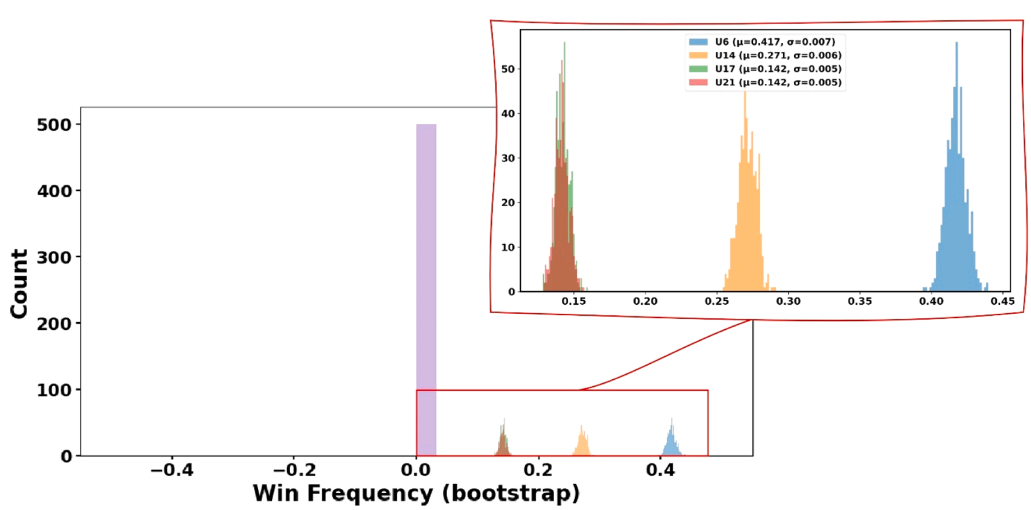

Fig. 28. Bootstrap win-frequency distributions for leading formulations.

Table 10
Bootstrap stability summary of ranking.

Sample ID	WF mean	WF std	Top K_{Prob}	Sample ID	WF mean	WF std	Top K_{Prob}
U6	0.4171744	0.00698729	1	U9	0	0	0
U14	0.2712972	0.0063025	1	U10	0	0	0
U17	0.1422224	0.004832223	1	U12	0	0	0
U21	0.1415996	0.004956604	1	U13	0	0	0
U16	0.0159772	0.001743158	0	U15	0	0	0
U11	0.0103568	0.001392801	0	U18	0	0	0
U5	0.0005956	0.000338793	0	U19	0	0	0
U8	0.0003864	0.000282516	0	U20	0	0	0
U24	0.0002056	0.000197101	0	U22	0	0	0
U2	0.0001848	0.000184848	0	U23	0	0	0
U3	0	0	0	U25	0	0	0
U4	0	0	0	U26	0	0	0
U7	0	0	0				

Table 11
Leave-one-out (LOO) winners and corresponding top 4 sets.

Left Out	Winner after LOO	Top 4 after LOO	Left Out	Winner after LOO	Top 4 after LOO
U2	U6	U6,U14, U17,U21	U15	U6	U6,U14, U21,U17
U3	U6	U6,U14, U21,U17	U16	U6	U6,U14, U21,U17
U4	U6	U6,U14, U21,U17	U17	U6	U6,U14, U21,U16
U5	U6	U6,U14, U21,U17	U18	U6	U6,U14, U17,U21
U6	U14	U14,U17, U21,U16	U19	U6	U6,U14, U21,U17
U7	U6	U6,U14, U17,U21	U20	U6	U6,U14, U17,U21
U8	U6	U6,U14, U21,U17	U21	U6	U6,U14, U17,U16
U9	U6	U6,U14, U17,U21	U22	U14	U14,U21, U17,U6
U10	U6	U6,U14, U17,U21	U23	U6	U6,U14, U21,U17
U11	U6	U6,U14, U21,U17	U24	U6	U6,U14, U17,U21
U12	U6	U6,U14, U21,U17	U25	U6	U6,U14, U17,U21
U13	U6	U6,U14, U21,U17	U26	U6	U6,U14, U21,U17
U14	U6	U6,U21, U17,U11			

the desirability, Taguchi, Pareto, or weight-uncertainty rankings. Replicated imaging using a predefined field-selection protocol and multiple independently sampled fields would be required for statistically supported formulation-wide microstructural comparisons.

The multi-response result is conditional on the included responses, desirability functions, normalization method, candidate set, and weight model. The symmetric Dirichlet distribution was used as an exchangeable reference scenario, it should not be interpreted as an empirically validated or uniquely non-informative prior. Alternative concentration vectors and response constraints may change the win frequencies and expected ranks. The bootstrap analysis quantifies numerical stability within the selected prior and does not remove this dependence. Application-specific decision analysis is therefore required before field implementation. Future work should replicate DSR testing, apply standardized short-and long-term aging, and evaluate rotational viscosity, storage stability, and asphalt-mixture performance.

5. Conclusions

This study investigated unaged bitumen modified with iron oxide, wollastonite, and microwave-activated crumb rubber using a Taguchi L25 design that varied both composition and processing conditions in a coordinated way. The combined evidence from conventional binder tests, DSR-based rheological measurements, FTIR, SEM/SEM-EDS, and the multi-response decision framework supports five main conclusions.

This study screened C320 binders modified with Fe_2O_3, wollastonite, and MACR across a Taguchi L25 composition–processing design. Within the observed dataset, all modified binders had higher softening points and lower penetration values than U1. MACR produced the largest descriptive shares of the observed MSCR and 60 °C viscoelastic variation, whereas mixing temperature and rotational speed produced the largest observed $N_{f,geo}$ contrasts. These contributions are descriptive screening quantities because the DSR specimens were not replicated.

Fourth, rutting improvement and LAS damage tolerance did not move together. U6 achieved $J_{nr,3.2} = 0.49kPa^{-1}$ and $R_{3.2} = 14.78\%$, but the neat binder retained the greatest LAS life at 15% strain. The reversal is consistent with a reinforcement/large-strain trade-off under the adopted LAS/VECD criterion, the present data do not distinguish among local stiffness contrast, incomplete dispersion, and model sensitivity as causes.

Fifth, FTIR showed no new dominant functional-group pattern, although minor oxidation or interfacial chemistry during hot blending cannot be excluded. Local SEM/EDS observations illustrated inorganic-phase organization within the analyzed fields, but the single-field descriptors do not establish bulk dispersion differences and were not used in the quantitative ranking or selection of U6.

FTIR showed no new dominant functional-group pattern that would indicate extensive formation of a new chemical network, however, limited oxidation, adsorption, or other interfacial chemistry during hot blending cannot be excluded.

Finally, the study demonstrated the practical value of integrating the Taguchi experimental design with a structured multi-response evaluation framework to reduce the extent of laboratory testing required. This approach enabled more efficient identification of suitable formulations, leading to savings in time, energy, and experimental cost.

Under the equal-weight baseline and uniform-simplex Dirichlet weight-sensitivity scenario, U6 (2% Fe_2O_3, 5% wollastonite, 12% MACR, 185 °C, 60 min, 6000 rpm) was the leading screening candidate, with $N_{f,geo} \approx 953$ and $D = 0.6869$ in addition to its MSCR performance. Its ranking is conditional on the tested binders, included responses, normalization procedure, candidate set, and selected weight model.

CRediT authorship contribution statement

Foad Ghasemi: Writing – original draft, Visualization, Investigation, Formal analysis, Data curation. **Ali Rajabipour:** Writing – review & editing, Validation, Supervision, Methodology, Conceptualization. **Ramin Shahbazi:** Writing – review & editing, Investigation, Formal analysis, Data curation. **Ehsan Yaghoubi:** Writing – review & editing, Validation, Supervision, Methodology, Formal analysis, Conceptualization. **Rudi van Staden:** Writing – review & editing, Validation, Supervision, Methodology, Conceptualization. **Ali Rahman:** Writing – review

& editing, Validation, Formal analysis, Conceptualization.

Declaration of Generative AI and AI-assisted technologies in the writing process

During the preparation of this work, the authors used ChatGPT (OpenAI) in order to improve the grammar, clarity, and overall readability of the manuscript. After using this tool, the author(s) reviewed and edited the content as needed and takes full responsibility for the content of the published article.

Declaration of Competing Interest

The authors declare that they have no known competing financial interests or personal relationships that could have appeared to influence the work reported in this paper.

Acknowledgements

This research was supported by an Australian Government Research Training Program (RTP) Scholarship [DOI: https://doi.org/10.82133/C42F-K220].

Data availability

Data will be made available on request.

References

[1] U. Bagampadde, U. Isacsson, B.M. Kiggundu, Classical and Contemporary Aspects of Stripping in Bituminous Mixes, Road. Mater. Pavement Des. 5 (1) (2004) 7–43, https://doi.org/10.1080/14680629.2004.9689961.
[2] M.C. Cavalli, W. Wu, L. Poulikakos, Bio-based rejuvenators in asphalt pavements: A comprehensive review and analytical study, J. Road. Eng. 4 (3) (2024) 282–291, https://doi.org/10.1016/j.jreng.2024.04.007.
[3] B. Ghorbani, E. Yaghoubi, P.L.P. Wasantha, R. Van Staden, M. Guerrieri, S. Fragomeni, Machine learning-based prediction of resilient modulus for blends of tire-derived aggregates and demolition wastes, Road. Mater. Pavement Des. 25 (4) (2024) 694–715, https://doi.org/10.1080/14680629.2023.2222176.
[4] F. Ghasemi, E. Yaghoubi, A. Rajabipour, R. Van Staden, A. Ghasemi, Climate-driven machine learning models for predicting asphalt pavement surface temperature for aging assessments, Eng. Appl. Artif. Intell. 167 (2026) 113897, https://doi.org/10.1016/j.engappai.2026.113897.
[5] R. Shahbazi, A. Rajabipour, E. Yaghoubi, M. Bazli, L.F. Herrera Diaz, B. Z. Dlugogorski, Rubber and plastic waste-modified asphalt binders and mixtures: Performance against environmentally induced distresses, J. Traffic Transp. Eng. (Engl. Ed. 12 (4) (2025) 876–906, https://doi.org/10.1016/j.jtte.2024.11.005.
[6] Ibrahim, B. Helwani, Z. Jahrizal, Nasruddin, A. Wiranata, E. Kurniawan, et al., Asphalt as a Plasticizer for Natural Rubber in Accelerated Production of Rubber-Modified Asphalt, Constr. Mater. 6 (1) (2026) 4, https://doi.org/10.3390/constrmater6010004.
[7] P.K. Athira, S.P. Atul Narayan, J. Murali Krishnan, P.K. Jain, Comparison of binder and mixture tests to characterize permanent deformation of elastomer and terpolymer modified binders, Constr. Build. Mater. 264 (2020) 120138, https://doi.org/10.1016/j.conbuildmat.2020.120138.
[8] H. Wang, X. Liu, S. Erkens, A. Skarpas, Experimental characterization of storage stability of crumb rubber modified bitumen with warm-mix additives, Constr. Build. Mater. 249 (2020) 118840, https://doi.org/10.1016/j.conbuildmat.2020.118840.
[9] F. Ghasemi, E. Yaghoubi, R. Van Staden, A. Rajabipour, Beyond oxidation: a new framework for understanding and effective simulation of asphalt aging in the era of climate-adaptive pavements, Road. Mater. Pavement Des. (2026), https://doi.org/10.1080/14680629.2026.2660314.
[10] Y. Li, G. Tian, W. Guo, Z. Wei, Z. Zhou, Z. Chen, et al., Fatigue resistance of asphalt and asphalt mixture incorporated with high-elasticity anti-rutting additive, Constr. Build. Mater. 459 (2025) 139730, https://doi.org/10.1016/j.conbuildmat.2024.139730.
[11] O. Xu, M. Li, S. Han, Y. Zhu, J. Zhang, Effect of diesel and microwave on the properties of crumb rubber and its modified binders, Constr. Build. Mater. 271 (2021) 121580, https://doi.org/10.1016/j.conbuildmat.2020.121580.
[12] S. Hosseinnezhad, S.F. Kabir, D. Oldham, M. Mousavi, E.H. Fini, Surface functionalization of rubber particles to reduce phase separation in rubberized asphalt for sustainable construction, J. Clean. Prod. 225 (2019) 82–89, https://doi.org/10.1016/j.jclepro.2019.03.219.
[13] W. Wu, W. Jiang, J. Xiao, D. Yuan, T. Wang, C. Xing, Analysis of thermal susceptibility and rheological properties of asphalt binder modified with microwave activated crumb rubber, J. Clean. Prod. 377 (2022) 134488, https://doi.org/10.1016/j.jclepro.2022.134488.
[14] L. Yin, X. Yang, A. Shen, H. Wu, Z. Lyu, B. Li, Mechanical properties and reaction mechanism of microwave-activated crumb rubber-modified asphalt before and after thermal aging, Constr. Build. Mater. 267 (2021) 120773, https://doi.org/10.1016/j.conbuildmat.2020.120773.
[15] A. Zare-Shahabadi, A. Shokuhfar, S. Ebrahimi-Nejad, Preparation and rheological characterization of asphalt binders reinforced with layered silicate nanoparticles, Constr. Build. Mater. 24 (7) (2010) 1239–1244, https://doi.org/10.1016/j.conbuildmat.2009.12.013.
[16] C. Kou, Z. Chen, A. Kang, M. Zhang, R. Wang, Rheological behaviors of asphalt binders reinforced by various fibers, Constr. Build. Mater. 323 (2022) 126626, https://doi.org/10.1016/j.conbuildmat.2022.126626.
[17] S. Karahancer, M. Enieb, M. Saltan, S. Terzi, E. Eriskin, A. Cengizhan, et al., Evaluating mechanical properties of bitumen and hot mix asphalt modified with nano ferric oxide, Constr. Build. Mater. 234 (2020) 117381, https://doi.org/10.1016/j.conbuildmat.2019.117381.
[18] J. Yu, Z. Ren, H. Yu, D. Wang, S. Svetlana, E. Korolev, Z. Gao, F. Guo, Modification of asphalt rubber with nanoclay towards enhanced storage stability, Materials 11 (11) (2018) 2093, https://doi.org/10.3390/ma11112093.
[19] N. Lushinga, Z. Dong, L. Cao, Evaluating the high-temperature properties and reaction mechanism of terminal blend rubber/nano silica composite modified asphalt using activated rubber, Nanomaterials 12 (24) (2022) 4388, https://doi.org/10.3390/nano12244388.
[20] S. Vigneswaran, J. Yun, M.S. Lee, S.J. Lee, Effect of nanocomposite clays on storage stability of rubberized binders under different curing and blending conditions, Int. J. Pavement Res. Technol. 19 (2026) 1313–1330, https://doi.org/10.1007/s42947-025-00499-3.
[21] H.M. Anaei, M. Khabiri, A. Mansourian, Effect of nanowollastonite wastes on bitumen and asphalt mixtures performance, Nanomater. Energy 13 (2) (2024) 64–75, https://doi.org/10.1680/jnaen.22.00017.
[22] N.A. Nair, V. Sairam, Research initiatives on the influence of wollastonite in cement-based construction material- A review, J. Clean. Prod. 283 (2021) 124665, https://doi.org/10.1016/j.jclepro.2020.124665.
[23] T. Giuffrè, M. Morreale, G. Tesoriere, S. Trubia, Rheological behaviour of a bitumen modified with metal oxides obtained by regeneration processes, Sustainability 10 (3) (2018) 604, https://doi.org/10.3390/su10030604.
[24] F. Li, X. Zhang, L. Wang, R. Zhai, The preparation process, service performances and interaction mechanisms of crumb rubber modified asphalt (CRMA) by wet process: A comprehensive review, Constr. Build. Mater. 354 (2022) 129168, https://doi.org/10.1016/j.conbuildmat.2022.129168.
[25] F.C.G. Martinho, J.P.S. Farinha, An overview of the use of nanoclay modified bitumen in asphalt mixtures for enhanced flexible pavement performances, Road. Mater. Pavement Des. 20 (3) (2019) 671–701, https://doi.org/10.1080/14680629.2017.1408482.
[26] C. Xin, Q. Lu, C. Ai, A. Rahman, Y. Qiu, Optimization of hard modified asphalt formula for gussasphalt based on uniform experimental design, Constr. Build. Mater. 136 (2017) 556–564, https://doi.org/10.1016/j.conbuildmat.2017.01.068.
[27] M. Hoseinpour-Lonbar, M.Z. Alavi, M. Palassi, Selection of asphalt mix with optimal fracture properties at intermediate temperature using Taguchi method for design of experiment, Constr. Build. Mater. 262 (2020) 120601, https://doi.org/10.1016/j.conbuildmat.2020.120601.
[28] J. Wang, K. Chen, X. Ye, J. Li, H. He, Y. Zhang, et al., Enhancing rheological properties and durability of asphalt binders with orthogonal-optimized composite modifier particles prepared via twin-screw extrusion: Performance and mechanisms, Case Stud. Constr. Mater. 24 (2026) e05897, https://doi.org/10.1016/j.cscm.2026.e05897.
[29] C. Panagiotopoulou, S. Tsivilis, G. Kakali, Application of the Taguchi approach for the composition optimization of alkali activated fly ash binders, Constr. Build. Mater. 91 (2015) 17–22, https://doi.org/10.1016/j.conbuildmat.2015.05.005.
[30] N. Saboo, P. Kumar, Study of flow behavior for predicting mixing temperature of bitumen, Constr. Build. Mater. 87 (2015) 38–44, https://doi.org/10.1016/j.conbuildmat.2015.04.001.
[31] J. Wititanapanit, J.S. Carvajal-Munoz, G. Airey, Performance-related and rheological characterisation of natural rubber modified bitumen, Constr. Build. Mater. 268 (2021) 121058, https://doi.org/10.1016/j.conbuildmat.2020.121058.
[32] Z. Kamali, E. Yaghoubi, M. Sandanayake, Mechanical, carbon emissions, and cost assessment of asphalt mixtures with incorporation of waste solar panel, Constr. Build. Mater. 495 (2025) 143733, https://doi.org/10.1016/j.conbuildmat.2025.143733.
[33] H.I. Al Abdul Wahhab, W. Rafiq, M. Khaliludin, Modeling and design optimization of dense graded modified crumb rubber asphalt mixtures using response surface methodology, Constr. Build. Mater. 435 (2024) 136895, https://doi.org/10.1016/j.conbuildmat.2024.136895.
[34] N.S.A. Yaro, M.B. Napiah, M.H. Sutanto, A. Usman, S.M. Saeed, Modeling and optimization of mixing parameters using response surface methodology and characterization of palm oil clinker fine modified bitumen, Constr. Build. Mater. 298 (2021) 123849, https://doi.org/10.1016/j.conbuildmat.2021.123849.
[35] S. Liu, W. Cao, S. Shang, H. Qi, J. Fang, Analysis and application of relationships between low-temperature rheological performance parameters of asphalt binders, Constr. Build. Mater. 24 (4) (2010) 471–478, https://doi.org/10.1016/j.conbuildmat.2009.10.015.
[36] M.M. Etghani, H. Boodaghi, Artificial Neural Networks and Taguchi Methods for Energy Systems Optimization: A Comprehensive Review, Energy Eng. 122 (11) (2025) 4385–4474, https://doi.org/10.32604/ee.2025.070668.

[37] Z. Kamali, M.M. Karimi, E. Ahmadi Dehaghi, H. Jahanbakhsh, Using electromagnetic radiation for producing reclaimed asphalt pavement (RAP) Mixtures: Mechanical, induced heating, and sustainability assessments, Constr. Build. Mater. 321 (2022) 126315, https://doi.org/10.1016/j.conbuildmat.2022.126315.
[38] M.W. Hisam, A.A. Dar, M.O. Elrasheed, M.S. Khan, R. Gera, I. Azad, The Versatility of the Taguchi Method: Optimizing Experiments Across Diverse Disciplines, J. Stat. Theory Appl. 23 (4) (2024) 365–389, https://doi.org/10.1007/s44199-024-00093-9.
[39] C.C. Ikeagwuani, D.C. Nwonu, Application of fuzzy logic and grey based Taguchi approach for additives optimization in expansive soil treatment, Road. Mater. Pavement Des. 23 (4) (2022) 849–873, https://doi.org/10.1080/14680629.2020.1847726.
[40] P.K. Ashish, D. Singh, S. Bohm, Evaluation of rutting, fatigue and moisture damage performance of nanoclay modified asphalt binder, Constr. Build. Mater. 113 (2016) 341–350, https://doi.org/10.1016/j.conbuildmat.2016.03.057.
[41] L.N. Lopes, M.M. De Farias, L.G.R. De Mello, Fatigue tests and damage analyses in modified binders and gap-graded asphalt mixtures with Reacted and Activated Rubber – RAR, Road. Mater. Pavement Des. 22 (7) (2021) 1616–1636, https://doi.org/10.1080/14680629.2019.1710553.
[42] S.H.R. Pasandideh, S.T.A. Niaki, Multi-response simulation optimization using genetic algorithm within desirability function framework, Appl. Math. Comput. 175 (1) (2006) 366–382, https://doi.org/10.1016/j.amc.2005.07.023.
[43] C.J. Slebi-Acevedo, P. Pascual-Muñoz, P. Lastra-González, D. Castro-Fresno, Multi-Response Optimization of Porous Asphalt Mixtures Reinforced with Aramid and Polyolefin Fibers Employing the CRITIC-TOPSIS Based on Taguchi Methodology, Materials 12 (22) (2019) 3789, https://doi.org/10.3390/ma12223789.
[44] Z. Liu, X. Ren, W. Du, Q. Li, D. Guo, M. Xu, et al., Optimization of Dosage for Asphalt Volatile Harmful Gas Inhibitor Using Multi-Response Satisfaction Function and Nonlinear Regression, Materials 19 (9) (2026) 1871, https://doi.org/10.3390/ma19091871.
[45] X. Yang, A. Shen, B. Li, H. Wu, Z. Lyu, H. Wang, et al., Effect of microwave-activated crumb rubber on reaction mechanism, rheological properties, thermal stability, and released volatiles of asphalt binder, J. Clean. Prod. 248 (2020) 119230, https://doi.org/10.1016/j.jclepro.2019.119230.
[46] C. Thodesen, K. Shatanawi, S. Amirkhanian, Effect of crumb rubber characteristics on crumb rubber modified (CRM) binder viscosity, Constr. Build. Mater. 23 (1) (2009) 295–303, https://doi.org/10.1016/j.conbuildmat.2007.12.007.
[47] A. Mitra, The Taguchi method, WIREs Comput. Stat. 3 (5) (2011) 472–480, https://doi.org/10.1002/wics.169.
[48] Standards Australia. AS 2341.12:2020, Methods of testing bitumen and related roadmaking products—Method 12: Determination of penetration, Standards Australia, Sydney, 2020.
[49] Standards Australia. AS 2341.18:2020, Methods of testing bitumen and related roadmaking products—Method 18: Determination of softening point, Standards Australia, Sydney, 2020.
[50] D. Mirzaiyan, M. Ameri, A. Amini, M. Sabouri, A. Norouzi, Evaluation of the performance and temperature susceptibility of gilsonite- and SBS-modified asphalt binders, Constr. Build. Mater. 207 (2019) 679–692, https://doi.org/10.1016/j.conbuildmat.2019.02.145.
[51] D. Kaya Özdemir, Temperature Susceptibility and Rheological Aging Characteristics of the Bitumen Having Different Penetration Grades, Black Sea J. Eng. Sci. 4 (4) (2021) 209–213, https://doi.org/10.34248/bsengineering.983109.
[52] R. Shahbazi, N. Ostadmoradi, A. Rajabipour, E. Yaghoubi, M. Bazli, K. Ghalandari Shamami, E. Shahryari, Mechanistic insights into modification, ageing, rheology, and intrinsic self-healing of hybrid recycled HDPE/crumb rubber-modified binders, Results Eng. 29 (2025) 108641, https://doi.org/10.1016/j.rineng.2025.108641.
[53] R. Shahbazi, N. Ostadmoradi, A. Rajabipour, E. Yaghoubi, M. Bazli, F. Ghasemi, Advancing durable and sustainable asphalt binder: Hybrid binders with recycled low-density polyethylene and crumb rubber, Constr. Build. Mater. 515 (2026) 145602, https://doi.org/10.1016/j.conbuildmat.2026.145602.
[54] American Association of State Highway and Transportation Officials, AASHTO T 315-22. Standard Method of Test for Determining the Rheological Properties of Asphalt Binder Using a Dynamic Shear Rheometer (DSR), AASHTO, Washington, DC, 2022.
[55] R. Shahbazi, N. Ostadmoradi, A. Rajabipour, E. Yaghoubi, M. Bazli, F. Ghasemi, Advancing durable and sustainable asphalt binder: Hybrid binders with recycled low-density polyethylene and crumb rubber, Constr. Build. Mater. 515 (2026) 145602, https://doi.org/10.1016/j.conbuildmat.2026.145602.
[56] American Association of State Highway and Transportation Officials, AASHTO T 350-19 (2023). Standard Method of Test for Multiple Stress Creep Recovery (MSCR) Test of Asphalt Binder Using a Dynamic Shear Rheometer (DSR), AASHTO, Washington, DC, 2023.
[57] American Association of State Highway and Transportation Officials, AASHTO T 391-20. Standard Method of Test for Estimating Fatigue Resistance of Asphalt Binders Using the Linear Amplitude Sweep, AASHTO, Washington, DC, 2020.
[58] ASTM International, ASTM E1252-98(2021). Standard Practice for General Techniques for Obtaining Infrared Spectra for Qualitative Analysis, ASTM International, West Conshohocken, PA, 2021, https://doi.org/10.1520/E1252-98R21.
[59] M. Mazumder, R. Ahmed, A. Wajahat Ali, S.J. Lee, SEM and ESEM techniques used for analysis of asphalt binder and mixture: A state of the art review, Constr. Build. Mater. 186 (2018) 313–329, https://doi.org/10.1016/j.conbuildmat.2018.07.126.
[60] M.B. Dillencourt, H. Samet, M. Tamminen, A general approach to connected-component labeling for arbitrary image representations, J. ACM 39 (2) (1992) 253–280, https://doi.org/10.1145/128749.128750.
[61] C.A. Schneider, W.S. Rasband, K.W. Eliceiri, NIH Image to ImageJ: 25 years of image analysis, Nat. Methods 9 (2012) 671–675, https://doi.org/10.1038/nmeth.2089.
[62] H.S. He, B.E. DeZonia, D.J. Mladenoff, An aggregation index to quantify spatial patterns of landscapes, Landsc. Ecol. 15 (7) (2000) 591–601, https://doi.org/10.1023/A:1008102521322.
[63] J. Butler, J. Jia, J. Dyer, Simulation techniques for the sensitivity analysis of multi-criteria decision models, Eur. J. Oper. Res. 103 (3) (1997) 531–546, https://doi.org/10.1016/S0377-2217(96)00307-4.
[64] T. Tervonen, G. van Valkenhoef, N. Baştürk, D. Postmus, Hit-And-Run enables efficient weight generation for simulation-based multiple criteria decision analysis, Eur. J. Oper. Res. 224 (3) (2013) 552–559, https://doi.org/10.1016/j.ejor.2012.08.026.
[65] J. Mazurek, D. Strzałka, On the Monte Carlo weights in multiple criteria decision analysis, PLoS. ONE 17 (10) (2022) e0268950, https://doi.org/10.1371/journal.pone.0268950.
[66] F. Pallasdies, P. Norton, J.H. Schleimer, S. Schreiber, Neural optimization: Understanding trade-offs with Pareto theory, Curr. Opin. Neurobiol. 71 (2021) 84–91, https://doi.org/10.1016/j.conb.2021.08.008.
[67] B. Hofko, A. Cannone Falchetto, J. Grenfell, L. Huber, X. Lu, L. Porot, et al., Effect of short-term ageing temperature on bitumen properties, Road. Mater. Pavement Des. 18 (sup2) (2017) 108–117, https://doi.org/10.1080/14680629.2017.1304268.
[68] Q. Liu, J. Wu, L. Xie, Z. Zhang, X. Ma, M. Oeser, Micro-scale investigation of aging gradient within bitumen film around air-binder interface, Fuel 286 (2021) 119404, https://doi.org/10.1016/j.fuel.2020.119404.
[69] F. Moreno-Navarro, M.C. Rubio-Gámez, A review of fatigue damage in bituminous mixtures: Understanding the phenomenon from a new perspective, Constr. Build. Mater. 113 (2016) 927–938, https://doi.org/10.1016/j.conbuildmat.2016.03.126.
[70] Y. Tan, J. Xie, W. Wang, P. Tataranni, C. Sangiorgi, Regeneration mechanisms of aged bitumen by rejuvenators: Insights from interfacial diffusion and structural deagglomeration, Constr. Build. Mater. 499 (2025) 143915, https://doi.org/10.1016/j.conbuildmat.2025.143915.
[71] X. Chen, L. Zhang, J. Liu, X. Xi, R. Yu, X. Cheng, Preparation and properties of synergistic activated rubber powder/SBS composite modified asphalt for waterproof coatings, Case Stud. Constr. Mater. 22 (2025) e04786, https://doi.org/10.1016/j.cscm.2025.e04786.
[72] A. Taheri, A. Khodaii, P. Hajikarimi, Correlations among chemical and rheological aging indices/indicators of asphalt binder at high temperatures, Sci. Rep. 16 (2026) 9186, https://doi.org/10.1038/s41598-026-40007-6.